González-Rubio, G; Mosquera, J; Kumar, V; Pedrazo-Tardajos, A; Llombart, P; Solís, DM; Lobato, I; Noya, EG; Guerrero-Martínez, A; Taboada, JM; Obelleiro, F; MacDowell, LG; Bals, S; Liz-Marzán, LM. ***Micelle-directed chiral seeded growth on anisotropic gold nanocrystals*** *Science, 2020, 368, 6498 (1472-1477).* DOI: 10.1126/science.aba0980

Micelle-directed chiral seeded-growth on anisotropic gold nanocrystals

Guillermo González-Rubio[1,+], Jesús Mosquera[1,+], Vished Kumar[1], Adrián Pedrazo-Tardajos[2], Pablo Llombart[3,4], Diego M. Solís[5], Ivan Lobato[2], Eva G. Noya[4], Andrés Guerrero-Martínez[3], José M. Taboada[6], Fernando Obelleiro[7], Luis G. MacDowell[3], Sara Bals[2*], Luis M. Liz-Marzán[1,8,9*]

[1] CIC biomaGUNE, Basque Research and Technology Alliance (BRTA), Paseo de Miramon 182, 20014 Donostia-San Sebastián, Spain

[2] Electron Microscopy for Materials Research (EMAT), University of Antwerp, Groenenborgerlaan 171, 2020 Antwerp, Belgium

[3] Departamento de Química Física I, Universidad Complutense de Madrid, Avenida Complutense s/n, 28040 Madrid, Spain

[4] Instituto de Química Física Rocasolano, CSIC, Calle Serrano 119, E-28006 Madrid, Spain

[5] Department of Electrical and Systems Engineering, University of Pennsylvania, Philadelphia, Pennsylvania 19104, USA

[6] Departamento de Tecnología de los Computadores y de las Comunicaciones, University of Extremadura, 10003 Cáceres, Spain

[7] Departamento de Teoría de la Señal y Comunicaciones, University of Vigo, 36301 Vigo, Spain

[8] Ikerbasque, Basque Foundation for Science, 48013 Bilbao, Spain

[9] CIBER de Bioingeniería, Biomateriales y Nanomedicina (CIBER-BBN), Paseo de Miramón 182, 20014 Donostia-San Sebastián, Spain

Abstract:

Surfactant-assisted seeded-growth of metal nanoparticles can be engineered to produce anisotropic gold nanocrystals with high chiroptical activity, through the templating effect of chiral micelles, formed in the presence of dissymmetric co-surfactants. Mixed micelles adsorb on gold nanorods forming quasi-helical patterns, which direct seeded growth into nanoparticles with pronounced morphological and optical handedness. Sharp chiral wrinkles lead to chiral plasmon modes with high dissymmetry factors (~0.20). Through variation of the dimensions of chiral wrinkles, the chiroptical properties can be tuned within the visible and near-infrared electromagnetic spectrum. The micelle-directed mechanism allows extension to other systems, such as the seeded growth of chiral platinum shells on gold nanorods. This approach provides a reproducible, simple and scalable method toward the fabrication of nanoparticles with high chiral optical activity.

One Sentence Summary: Seeded growth of gold nanorods in the presence of micelles with chiral co-surfactants results in nanoparticles with high chiroplasmonic activity.

Chirality is a key signature of nature that can be found across length scales, from subatomic particles, through molecules and biological systems, to galaxies (*1–3*). Imparting handedness to selected materials may provide important advantages in terms of their interaction with living organisms, as well as allow the development of enantioselective catalysts or obtain spin selectivity in electron transport (*4–6*). For example, the demonstration of chiral plasmon modes in noble metal nanocrystals (NCs) has drawn interest in the field of metamaterials and the design of enantioselective sensing probes (*7–9*). The fabrication of plasmonic nanostructures has thus become an active field of research *(10-16).* However, growing crystalline noble metals with dissymmetric morphology is challenging (*10–12*). The formation of chiral plasmonic nanomaterials is usually achieved by means of the assembly of achiral plasmonic gold and silver nanoparticles (NPs) with molecular templates such as DNA, proteins, or polymeric fibers (*13–15*). Although lithographic approaches have been successfully applied to fabricate chiral gold NPs, their scalability remains limited (*9*, *16*).

Advances in the colloidal synthesis of noble metal NPs achieved during the past decades point toward realistic prospects for the production of plasmonic NCs with diverse morphologies, including chiral ones (*17–19*). The presence of chiral amino acids during growth can guide the formation of NCs with distinct handedness. The most prominent example is the synthesis of helicoidal nanostructures assisted by cysteine and glutathione. The enantioselective interaction of amino acids with chiral geometrical elements naturally appearing at particular NC facets has been claimed to induce the observed shape evolution into twisted geometries with high dissymmetry factors (*11,20*).

In addition to chiral additives, the synthesis of colloidal chiral NPs requires surface ligands that prevent undesired aggregation (*11*, *21*). However, most of these capping agents also play a role in the growth process and the resulting NC morphology (*17*, *22*). Among the wide variety of ligands used for the synthesis of noble metal NCs, quaternary alkylammonium halide (CTAX, X = Cl, Br) surfactants are some of the most extensively investigated ones. Through the adsorption of CTAX micellar aggregates on certain crystallographic facets, a wide variety of nanoparticle morphologies have been obtained, including nanorods, nanotriangles, and Platonic geometries (*17–19*, *22–24*).

Recently, the addition of co-surfactants such as aromatic molecules, fatty acids, or long chain alkyl alcohols, has been shown to further improve the quality of colloidal gold NPs, and of nanorods in particular (*25–27*). The ability of cosurfactants to intercalate within CTAX surfactant aggregates has been proposed to increase the rigidity of the micelles, induce phase transitions, or both. Interestingly, the impact of co-surfactants on the aggregation behavior of surfactant molecules can also be extended to the formation of chiral micelles. For example, (*R*)-(+)-1,1′-bi(2-naphthol) ((*R*)-BINOL), a co-surfactant with axial chirality (i.e., atropisomerism), can induce the formation of chiroptically active giant worm-like micelles (*28*).

Considering the role of surfactants on the synthesis of gold NCs and the possibility of producing chiral micelles in the presence of BINOL-like co-surfactants, we envisioned the surfactant-assisted seeded-growth of chiral gold NCs. We hypothesized that elongated rod-like particles would have the ideal shape to guide the adsorption of twisted, worm-like micelles on the gold surface into helix-like chiral structures. To investigate both hypotheses, we first carried out a computational analysis on an ideal system comprising cetyltrimethyl ammonium chloride (CTAC) and BINOL. Molecular dynamics (MD) simulations revealed that BINOL molecules induced the assembly of surfactants into chiral wormlike aggregates.

Such elongated micelles tend to coil around gold nanorods, which can thus be considered as templates for the seeded growth of anisotropic NPs with chiral features.

Although experimental evidence of the proposed idea was obtained using BINOL as a co-surfactant, the results of chiral growth were largely improved by using its derivative (*R*)-(+)-1,1′-binaphthyl-2,2′-diamine ((*R*)-BINAMINE)). The growth of plasmonic gold nanorods patterned with a complex chiral surface was indeed confirmed by high-angle annular dark-field scanning transmission electron microscopy (HAADF-STEM) tomography. By tuning the dimensions of the final nanostructures, high anisotropy factors (g-factor ~0.20) were achieved within a wide wavelength range (from 500 to beyond 1350 nm). Theoretical modeling of the optical properties highlights the importance of growing well-defined chiral wrinkles to obtain intense circular dichroism (CD) responses.

MD simulations confirmed that, in the presence of BINOL as a co-surfactant, CTAC can form giant cylindrical micelles that span across the simulation boxes (i.e., up to 60 nm in length; Fig. 1A, fig. S1). Regarding their chiral nature, we observed that unit vectors between the local micellar center and the principal micellar axis were distributed helically; the handedness being dictated by the choice of co-surfactant stereoisomer. This effect can be shown by measuring the average angle formed between pairs of vectors (fig. S2). An achiral helix does not have any tendency to coil into a particular direction, so the angle formed between such vectors averages out to zero.

In our simulations, the average angles not only were finite but appeared sinusoidally correlated and displayed a well-defined handedness (Fig. 1B). Because of the marked atropisomerism of BINOL, we can assume that it could induce helical chirality onto the surfactant aggregates, likely by a sergeants and soldiers mechanism where a chiral molecule directs many achiral molecules or atoms (*29, 30)*. In this case, the adsorbed chiral micelles would assist chirality transfer during further deposition of metal atoms onto the nanorods surface.

We tested this effect by simulating a gold nanorod, immersed in an aqueous mixed solution of CTAB and BINOL. Visual inspection of the simulation results revealed that CTAB and BINOL adsorb into wormlike micelles coiled around the gold nanorod surface (Fig. 1, C and D). Although no preferred orientation of the assembly was observed by the use of different BINOL enantiomers in this case, in the absence of co-surfactant, the coillike morphology was largely lost. Instead, small aggregates and a high fraction of individual surfactant molecules would adsorb on the gold surface (fig. S3). The simulations indicate that chiral wormlike micelles likely formed first and subsequently adsorbed onto the gold nanorod. Thus, a complex cooperative chiral transfer mechanism would convey the atropisomerism from BINOL into the giant micelles and ultimately to gold nanorods.

On the basis of the simulation results, we implemented experimentally the growth of chiral nanorods. (*R*)-BINOL was solubilized by surfactant micelles in aqueous solution, at an optimum molar ratio of 40, and used to template the growth of preformed gold nanorods (130 ± 10 nm long, 29 ± 2 nm thick, see Fig. 2A and SM for details; note that BINOL is insoluble in water in the absence of surfactant). Preliminary characterization by CD spectroscopy revealed the appearance of moderate chiral localized surface plasmon resonance (LSPR) bands (figs. S4 and S5, g-factor ~ 0.002). HAADF-STEM analysis of the NPs grown in the (*R*)-BINOL/surfactant mixture revealed a complex morphology characterized by the presence of wrinkles on the nanorod surface (Fig. 2B and fig. S4). Previous theoretical and experimental studies demonstrated that intense CD responses are exhibited by NPs with distinct chiral distortions, stellated-like morphologies, or both (*9*, *11*, *31*).

Encouraged by the appearance of plasmonic bands in the CD spectra, our efforts focused on improving chiral seeded growth. We hypothesized that the use of stronger stabilizing agents would help directing the growth of more structured chiral wrinkles (*32*). We investigated (*R*)-BINAMINE, an analog of (*R*)-BINOL in which the hydroxyl functionalities are replaced by amine moieties. Although the interaction of amines with gold surfaces is moderately strong (Au–N bond energy ~ 6 kcal/mol), the presence of two amines in a chelating configuration should ensure a greater affinity (*33*, *34*). MD simulations of the BINAMINE/CTAC system confirmed the formation of chiral wormlike aggregates, similar to those for BINOL/CTAC, with a helical distribution of unit vectors (fig. S6). HAADF-STEM analysis of the particles obtained by seeded-growth in (*R*)-BINAMINE/CTAC revealed the presence of gold nanorods displaying a highly complex surface morphology, resembling an intricate network of wrinkles (Fig. 2C, and figs. S7 to 10). Scanning electron microscopy (SEM) imaging of the same NPs also revealed a complex surface structure (fig. S11).

Notwithstanding, proper understanding of such complex structures demands a more detailed characterization than that provided by either HAADF-STEM or SEM, which only retrieve 2D and surface information, respectively. We used HAADF-STEM tomography, which has been shown to be a powerful technique to investigate the three-dimensional morphology of complex NCs. We prepared similar particles, but with increasing dimensions, using 130 nm by 29 nm gold nanorods as seeds and characterized by HAADF-STEM (see SM for synthetic details). Electron tomography reconstructions of nanorods with the smallest degree of growth, i.e. 165 nm long and 73 nm thick, revealed the presence of sharp wrinkles oriented in a seemingly radial direction and displaying tilt angles between 0° and 45° with respect to the short axis (Fig. 2D). Detailed analysis of the internal structure suggested that the wrinkles grew from the surface of the gold nanorod seed, in a quasi-radial direction, up to ~15 to 20 nm in height and with a constant width of 3 to 4 nm. The average intergroove separation was measured to be 2 to 3 nm (Fig. 2E), which is near the 3.75 nm width of wormlike micelles obtained from MD simulations. This finding would point to a micelle-directed chiral growth of the gold nanorods, as we initially hypothesized.

The width of the wrinkles was compatible with the diffusion of metal ion-loaded CTAC micelles from solution (*35*), leading to reduction at available gold sites in between CTAC/BINAMINE micelles on the nanorod surface. By varying the concentration of nanorod seeds in the growth mixture, chiral nanorods were obtained with increased dimensions of 210 nm in length and 112 nm in thickness, and their surface was more entangled (Fig. 2F). Nonetheless, the presence of tilted wrinkles was still visible and angles between 0° and 45° were again observed (between 0° and -45° in the case of (*S*)-BINAMINE, fig. S9). Analysis of the internal structure revealed wrinkles of ca. 35 to 45 nm in height and a similar width to those in the smaller rods (Fig. 2G). Finally, even larger chiral nanorods (270 nm long and 175 nm thick) were investigated. Although the surface appeared more undefined in this case (Fig. 2H), analysis of the internal structure showed the characteristic features described for the previous samples (Fig. 2I). For completeness, 3D animations of all discussed systems are provided as Supplementary Material (Movies S1 to S48).

Diffraction of ideal helical structures results in X-shaped patterns (*36*, *37*). Thus, we applied fast Fourier transformations (FFT) to our 3D reconstructions. We exemplify this analysis with chiral nanorods of 210 nm by 112 nm (Fig. 3, A and B), from which the 3D FFT indeed shows an X-shaped pattern (Fig. 3C); further details are provided in the SM, as well as comparison with an idealized model (fig. S12), with a smooth nanorod (fig. S13) and with a BINOL-grown nanorod (fig. S13). Next, the spots in reciprocal space can be linked to the corresponding features in real space by manually segmenting the 3D FFT to minimize noise. By using the segmented 3D FFT as a mask (see details in SM), an inverse FFT (*38*)

was computed and overlayed (pink fringes) with the original reconstruction, as exemplified in Fig. 3D, so that the helical features are visually highlighted. Although the use of a 3D FFT does not provide a quantitative value such as e.g. the Hausdorff chirality measure (*39*), it provides a qualitative and visual way to estimate the presence of chiral features. The inverse FFT enables direct location of specific periodicities at a local level.

Fringes with a right handed angle can be seen in Fig. 3D, and the wrinkles growing on the sides of the gold nanorod seeds seemed to display a better-defined chiral arrangement than those located at the hemispherical tips. The observation of a curvature-dependent growth was confirmed by a control experiment, in which seeded-growth was carried out on 30 nm gold nanospheres (figs. S14 and S15) Although some chiral features could still be observed, the spheres yielded a more random wrinkle organization, as revealed by the corresponding HAADF-STEM tomography reconstruction (Fig. 2, J and K) and further supported by their 3D FFT and corresponding inverse FFT (fig. S14). Accordingly, more intense plasmonic CD bands were recorded when gold nanorods were used as seeds (g-factor ~0.2, Fig. 4A) as compared to spheres (g-factor ~0.003, fig S15).

Additional evidence behind the general validity of this chiral growth method and the proposed mechanism was provided by experiments in which we varied the nature of the metal deposited during seeded growth. We thus implemented the seeded growth of Pt on BINOL/CTAC-covered gold nanorods, using identical dimensions and similar growth conditions. Representative results are shown in Fig. 3, E to H, show that seeded growth resulted in strikingly regular wrinkled platinum coating. The smaller dimensions of the wrinkles, as well as the different electron configuration between platinum and gold (see a 3D EDX reconstruction in fig. 3E, right), allow a better distinction of the obtained pattern. Although the tilting angle is obviously lower than that measured for gold, a helical character is demonstrated by the 3D-FFT analysis (Fig. 3G and H). Unfortunately, the lossy character of platinum does not allow to record meaningful plasmonic optical activity for these samples.

We next demonstrate that the optical activity (CD bands) can be modulated by varying the dimensions of chiral nanorods (by varying the amount of seeds in the growth solution). In all cases, an intense negative Cotton effect was recorded for the (*R*)-enantiomer (*29*). As the size of the nanorods was increased from 165 nm by 73 nm to 270 nm by 175 nm, the positive band redshifted from 700 up to 1300 nm, and the maximum of the negative band shifted from 1100 to beyond 1350 nm (fig. S16). Analysis of the anisotropy factor showed values ranging from 0.1 to 0.2 (Fig. 4A), which are among the highest values reported for colloidal plasmonic NPs in the visible and NIR ranges (*10*, *11*). By extending the analysis further into the NIR, up to the limit of our CD spectrometer (1600 nm), we recorded even higher dissymmetry factors of 0.25 to 0.28 (fig. S17). However, the noise in the 1400 to 1500 nm range precluded us from obtaining more compelling evidence to confirm the precise values.

When gold nanorods of different dimensions and degrees of anisotropy were used to seed the chiral growth (fig. S18 and S19), similar trends in optical activity were observed. However, the anisotropy factor was influenced by the nanorod dimensions. In general, slightly lower g-factor values were obtained when shorter and thinner gold nanorods were used as seeds (100 nm by 12 nm; i.e., higher aspect ratio), while a decrease was observed for seeds with similar length to the optimal one but thicker in diameter (135 nm by 52 nm; i.e., lower aspect ratio).

The relation between the chiral features observed by electron microscopy and the chiroptical activity measured by CD spectroscopy was further investigated by electromagnetic modeling. We used an accurate full-wave solver based on Maxwell's surface integral

equations and the method of moments to model the plasmonic properties of chiral gold nanorods (see SM for details) (*40-42*). Three-dimensional computer-aided design (CAD) models were constructed on the basis of the information provided by the experimental electron tomography reconstructions (Fig. 4B). Although suitable reproduction of the observed morphologies appeared challenging, given the intricate network of wrinkles covering the chiral gold nanorod surface, we created models for the three different dimensions characterized by electron microscopy: 165 nm by 73 nm, 210 nm by 112, and 270 nm by 175 nm. To mimic the regions with wrinkles displaying different angles, each rod was built with sixteen helices having four leveled and four inclined steps per pitch (pitch of 90 nm). The wrinkle width was fixed at 3.5 nm and the separation distance between wrinkles was 2.5 nm.

The simulations revealed chiral plasmonic bands that shifted toward longer wavelengths with increasing nanorod dimensions, in agreement with the experimental results (Fig. 4C, fig. S20 to S22). Differences in the anisotropy factors can be attributed to the polydispersity in size and shape of the real sample, as well as the difficulty in modeling the exact morphology of the NPs. Overall, our theoretical model confirmed the origin of the plasmonic chiroptical activity and the importance of sharp wrinkles for the emergence of strong CD responses. Replacement of BINAMINE by L-cysteine did not induce any clear modification on the CD signal obtained for chiral nanorods synthesized with either (*R*)-BINAMINE or (*S*)-BINAMINE. A substantial modification would be expected if the chiroptical properties would stem from the coupling of the chiral molecules with the NP plasmon, rather than from the chiral structural features (fig. S23). (*43*)

We have experimentally demonstrated that chiral gold nanostructures can be readily obtained by seeded-growth of gold nanorods in BINOL/surfactant mixtures, whereas NP colloids with intense CD responses were obtained using BINAMINE/surfactant mixed micelles. The chiroptical properties stem from the formation and stabilization of steep chiral wrinkles. These findings point to a dual role of mixed micelles: (i) templating the growth of steep wrinkles and (ii) the subsequent stabilization of such morphological features.

We propose that the formation of wrinkles during seeded-growth can be explained by the presence of elongated micelles coiled on the gold nanorod seeds, which act as patterns directing the diffusion of micellar aggregates containing gold ions, from the aqueous solution toward the core NC at intermicellar regions. Indeed, the size of micelles in solution would fit the interwrinkle distance on the nanorod surface. However, wrinkle formation is only induced when the rate of gold ion deposition is faster than their diffusion on the surface (*44*). We observed that, upon lowering the concentration of reducing agent (ascorbic acid, from 160 down to 1.6 mM), the CD intensity decreased by an order of magnitude and less defined surface roughness was observed in STEM (fig. S24).

An additional source of surface stabilization is required to preserve the wrinkles after growth. In this case, BINAMINE plays such a role during the growth process, likely because of its two amine moieties in chelating conformation (*33*). When one of the amine groups in BINAMINE was replaced by a hydroxyl moiety, the passivation effect was suppressed and the growth of chiral features was hindered, which resulted in a decrease of CD intensity (fig. S25). Once the growth is completed, addition of a stronger stabilizing agent (e.g., cysteine) is necessary because the adsorption of surfactant micelles is not sufficiently strong and the nanoparticles may slowly reshape, as reflected by the loss of chiroptical properties (fig. S26).

The approach described here for the synthesis of chiral plasmonic anisotropic nanocrystals is simple, reproducible, and holds great potential for large scale production, intrinsic to colloid chemistry methods. Compared with the growth of inorganic chiral

nanostructures based on the direct chemisorption of small additives on the NC surface to induce chiral growth, the micelle-directed growth method relies on the ability of the chiral-co-surfactant to direct the formation of helical micelles. Such supramolecular assemblies have sufficient interaction points with the NPs to effectively transfer their chirality to the NPs during the growth step through a multivalency effect.

References

1. J. Bailey, A. Chrysostomou, J. H. Hough, T. M. Gledhill, A. McCall, S. Clark, F. Ménard, M. Tamura, Circular Polarization in Star- Formation Regions: Implications for Biomolecular Homochirality. *Science* **281**, 672–674 (1998).

2. L. A. Hodge, F. B. Dunning, G. K. Walters, R. H. White, G. J. Schroepfer, Degradation of DL-Leucine with Longitudinally Polarised Electrons. *Nature* **280**, 250–252 (1979).

3. R. E. Franklin, R. G. Gosling, Molecular Configuration in Sodium Thymonucleate. *Nature* **171**, 740–741 (1953).

4. D. Hanein, B. Geiger, L. Addadi, Differential Adhesion of Cells to Enantiomorphous Crystal Surfaces. *Science* **263**, 1413–1416 (1994).

5. T. P. Yoon, E. N. Jacobsen, Privileged Chiral Catalysts. *Science* **299**, 1691–1693 (2003).

6. K. Ray, S. P. Ananthavel, D. H. Waldeck, R. Naaman, Asymmetric Scattering of Polarized Electrons by Organized Organic Films of Chiral Molecules. *Science* **283**, 814–816 (1999).

7. A. S. Karimullah, C. Jack, R. Tullius, V. M. Rotello, G. Cooke, N. Gadegaard, L. D. Barron, M. Kadodwala, Disposable Plasmonics: Plastic Templated Plasmonic Metamaterials with Tunable Chirality. *Adv. Mater*. **27**, 5610–5616 (2015).

8. C. Hao, L. Xu, H. Kuang, C. Xu, Artificial Chiral Probes and Bioapplications. *Adv. Mater.* **32**, 1802075 (2020).

9. J. K. Gansel, M. Thiel, M. S. Rill, M. Decker, K. Bade, V. Saile, G. von Freymann, S. Linden, M. Wegener, Gold Helix Photonic Metamaterial as Broadband Circular Polarizer. *Science* **325**, 1513–1515 (2009).

10. M. Hentschel, M. Schäferling, X. Duan, H. Giessen, N. Liu, Chiral Plasmonics. *Science Adv*. **3**, e1602735 (2017).

11. H.-E. Lee, H.-Y. Ahn, J. Mun, Y. Y. Lee, M. Kim, N. H. Cho, K. Chang, W. S. Kim, J. Rho, K. T. Nam. Amino-Acid- and Peptide-Directed Synthesis of Chiral Plasmonic Gold Nanoparticles. *Nature* **556**, 360–365 (2018).

12. G. Zheng, Z. Bao, J. Pérez-Juste, R. Du, W. Liu, J. Dai, W. Zhang, L. Y. S. Lee, K.-Y. Wong, Tuning the Morphology and Chiroptical Properties of Discrete Gold Nanorods with Amino Acids. *Angew. Chem. Int. Ed*. **57**, 16452–16457 (2018).

13. A. Kuzyk, R. Schreiber, Z. Fan, G. Pardatscher, E.-M. Roller, A. Högele, F. C. Simmel, A. O. Govorov, T. Liedl. DNA-Based Self-Assembly of Chiral Plasmonic Nanostructures with Tailored Optical Response. *Nature* **483**, 311–314 (2012).

14. C.-L. Chen, P. Zhang, N. L. Rosi, A New Peptide-Based Method for the Design and Synthesis of Nanoparticle Superstructures: Construction of Highly Ordered Gold Nanoparticle Double Helices. *J. Am. Chem. Soc.* **130**, 13555–13557 (2008).

15. A. Guerrero-Martínez, B. Auguié, J. L. Alonso-Gómez, Z. Džolić, S. Gómez-Graña, M. Žinić, M. M. Cid, L. M. Liz-Marzán, Intense Optical Activity from Three-Dimensional Chiral Ordering of Plasmonic Nanoantennas. *Angew. Chem. Int. Ed.* **50**, 5499–5503 (2011).

16. A. G. Mark, J. G. Gibbs, T.-C. Lee, P. Fischer, Hybrid Nanocolloids with Programmed Three-Dimensional Shape and Material Composition. *Nat. Mater.* **12**, 802–807 (2013).

17. Y. Xia, Y. Xiong, B. Lim, S. E. Skrabalak, Shape-Controlled Synthesis of Metal Nanocrystals: Simple Chemistry Meets Complex Physics? *Angew. Chem. Int. Ed*. **48**, 60–103 (2009).

18. B. Nikoobakht, M. A. El-Sayed, Preparation and Growth Mechanism of Gold Nanorods (NRs) Using Seed-Mediated Growth Method. *Chem. Mater.* **15**, 1957–1962 (2003).

19. S. Hong, K. L. Shuford, S. Park. Shape Transformation of Gold Nanoplates and their Surface Plasmon Characterization: Triangular to Hexagonal Nanoplates. *Chem. Mater.* **23**, 2011–2013 (2011).

20. H.-E. Lee, R. M. Kim, H.-Y. Ahn, Y. Y. Lee, G. H. Byun, S. W. Im, J. Mun, J. Rho, K. T. Nam. Cysteine-Encoded Chirality Evolution in Plasmonic Rhombic Dodecahedral Gold Nanoparticles. *Nat. Comm.* **11**, 263 (2020).

21. C. A. S. Batista, R. G. Larson, N. A. Kotov. Nonadditivity of Nanoparticle Interactions. *Science* **350**, 1242477 (2015).

22. M. L. Personick, C. A. Mirkin, Making Sense of the Mayhem behind Shape Control in the Synthesis of Gold Nanoparticles. *J. Am. Chem. Soc.* **135**, 18238–18247 (2013).

23. S. E. Lohse, N. D. Burrows, L. Scarabelli, L. M. Liz-Marzán, C. J. Murphy, Anisotropic Noble Metal Nanocrystal Growth: The Role of Halides. *Chem. Mater.* **26**, 34–43 (2014).

24. S. K. Meena, M. Sulpizi, From Gold Nanoseeds to Nanorods: The Microscopic Origin of the Anisotropic Growth. *Angew. Chem. Int. Ed.* **55**, 11960–11964 (2016).

25. L. Scarabelli, M. Grzelczak, L. M. Liz-Marzán, Tuning Gold Nanorod Synthesis through Prereduction with Salicylic Acid. *Chem. Mater.* **25**, 4232–4238 (2013).

26. X. Ye, C. Zheng, J. Chen, Y. Gao, C. B. Murray, Using Binary Surfactant Mixtures to Simultaneously Improve the Dimensional Tunability and Monodispersity in the Seeded Growth of Gold Nanorods. *Nano Lett.* **13**, 765–771 (2013).

27. G. González-Rubio, V. Kumar, P. Llombart, P. Díaz-Núñez, E. Bladt, T. Altantzis, S. Bals, O. Peña-Rodríguez, E. G. Noya, L. G. MacDowell, A. Guerrero-Martínez, L. M.

Liz-Marzán, Disconnecting Symmetry Breaking from Seeded Growth for the Reproducible Synthesis of High Quality Gold Nanorods. *ACS Nano* **13**, 4424–4435 (2019).

28. T. H. Ito, A. G. Salles, J. P. Priebe, P. C. M. L. Miranda, N. H. Morgon, D. Danino, G. Mancini, E. Sabadini, Generation of a Chiral Giant Micelle. *Langmuir* **32**, 8461–8466 (2016).

29. M. M. Green, M. P. Reidy, R. D. Johnson, G. Darling, D. J. O'Leary, G. Willson. Macromolecular Stereochemistry: The Out-of-Proportion Influence of Optically Active Comonomers on the Conformational Characteristics of Polyisocyanates. The Sergeants and Soldiers Experiment. *J. Am. Chem. Soc.* **111**, 6452-6454 (1989).

30. E. E. Greciano, J. Calbo, J. Buendía, J. Cerdá, J. Aragó, E. Ortí, L. Sánchez, Decoding the Consequences of Increasing the Size of Self-Assembling Tricarboxamides on Chiral Amplification. *J. Am. Chem. Soc.* **141**, 7463–7472 (2019).

31. Z. Fan, A. O. Govorov, Chiral Nanocrystals: Plasmonic Spectra and Circular Dichroism. *Nano Lett.* **12**, 3283–3289 (2012).

32. J. Zhang, M. R. Langille, M. L. Personick, K. Zhang, S. Li, C. A. Mirkin, Concave Cubic Gold Nanocrystals with High-Index Facets. *J. Am. Chem. Soc.* **132**, 14012–14014 (2010).

33. S. Engel, E.-C. Fritz, B. J. Ravoo, New Trends in the Functionalization of Metallic Gold: From Organosulfur Ligands to N-Heterocyclic Carbenes. *Chem. Soc. Rev.* **46**, 2057–2075 (2017).

34. B.-K. Pong, J.-Y. Lee, B. L. Trout, First Principles Computational Study for Understanding the Interactions between ssDNA and Gold Nanoparticles: Adsorption of Methylamine on Gold Nanoparticulate Surfaces. *Langmuir* **21**, 11599–11603 (2005).

35. J. Pérez-Juste, L.M. Liz-Marzán, S. Carnie, D.Y.C. Chan, P. Mulvaney. Electric Field Directed Growth of Gold Nanorods in Aqueous Surfactant Solutions. *Adv. Funct. Mater.* **14**, 571–579 (2004).

36. H. Zhu, K. Suenaga, A. Hashimoto, K. Urita, K. Hata, S. Ijima, Atomic-Resolution Imaging of the Nucleation Points of Single-Walled Carbon Nanotubes. *Small* **1**, 1180–1183 (2005).

37 M. Gailhanou, J. M. Roussel, Diffraction from Twisted Nanowires: Helicity Revealed by Anisotropy. *J. Appl. Cryst.* **24**, 14012–14014 (2003).

38. M. C. Scott, C.-C. Chen, M. Mecklenburg, C. Zhu, R. Xu, P. Ercius, U. Dahmen, B. C. Regan, J. Miao, Electron Tomography at 2.4-Ångström Resolution. *Nature* **483**, 444–447 (2012).

39. J.-Y. Kim, J. Yeom, G. Zhao, H. Calcaterra, J. Munn, P. Zhang, N. Kotov, Assembly of Gold Nanoparticles into Chiral Superstructures Driven by Circularly Polarized Light. *J. Am. Chem. Soc.* **141**, 11739–11744 (2019).

40. D. M. Solís, J. M. Taboada, F. Obelleiro, L. M. Liz-Marzán, F. J. García de Abajo, Toward Ultimate Nanoplasmonics Modeling. *ACS Nano* **8**, 7559–7570 (2014).

41. J. M. Taboada, J. Rivero, F. Obelleiro, M. G. Araújo, L. Landesa. Method-of-Moments Formulation for the Analysis of Plasmonic Nano-Optical Antennas. *J. Opt. Soc. Am. A* **28**, 1341–1348 (2011).

42. D. M. Solís, J. M. Taboada, F. Obelleiro. Surface Integral Equation-Method of Moments with Multiregion Basis Functions Applied to Plasmonics. *IEEE Trans. Antennas Propag.* **63**, 2141–2152 (2015).

43. A. O. Govorov, Z. Fan, P. Hernandez, J. M. Slocik, R. R. Naik, Theory of Circular Dichroism of Nanomaterials Comprising Chiral Molecules and Nanocrystals: Plasmon Enhancement, Dipole Interactions, and Dielectric Effects. *Nano Lett.* **10**, 1374–1382 (2010).

44. Y. Xia, K. D. Gilroy, H.-C. Peng, X. Xia, Seed-Mediated Growth of Colloidal Metal Nanocrystals. *Angew. Chem. Int. Ed.* **56**, 60–95 (2017).

45. T. Altantzis, I. Lobato, A. De Backer, A. Béché, Y. Zhang, S. Basak, M. Porcu, Q. Xu, A. Sánchez-Iglesias, L. M. Liz-Marzán, G. Van Tendeloo, S. Van Aert, S. Bals. Three-Dimensional Quantification of the Facet Evolution of Pt Nanoparticles in a Variable Gaseous Environment. *Nano Letters*. **19**, 477-481 (2019).

46. Zanaga, T. Altantzis, L. Polavarapu, L. M. Liz-Marzán, B. Freitag, S. Bals. A new method for quantitative XEDS tomography of complex heteronanostructures. *Particle & Particle Systems Characterization*, **33**, 396-403 (2016).

47. Goris, W. Van den Broek, K. J. Batenburg, H. H. Mezerji, S. Bals. Electron tomography based on a total variation minimization reconstruction technique. *Ultramicroscopy*, **113**, 120-130 (2012).

48. C. Hanske, G. González-Rubio, C. Hamon, P. Formentín, E. Modin, A. Chuvilin, A. Guerrero-Martínez, L. F. Marsal, L. M. Liz-Marzán. Large-Scale Plasmonic Pyramidal Supercrystals via Templated Self-Assembly of Monodisperse Gold Nanospheres. *J. Phys. Chem. C*. **121**, 10899–10906 (2017).

49. P. Llombart, M. Alzola-Palafox, L. G. MacDowell, E. G. Noya. Structural Transitions and Bilayer Formation of CTAB Aggregates. *Colloids Surf. A* **580**, 123730 (2019).

50. M. A. K. Zuo, L. Breeze, M. Stroet, M. Poger, D. Nair, P. C. Oostenbrink, A.E.C. Mark. An Automated Force Field Topology Builder (ATB) and Repository: Version 1.0. *J. Chem. Theory Comput.* **7,** 4026–4037 (2011).

51. L. Martínez ,R. Andrade, E.G. Birgin, J.M. Martínez. PACKMOL: A Package for Building Initial Configurations for Molecular Dynamics Simulations. *J. Comput. Chem*. **30**, 2157–2164 (2009).

52. G. Bussi, D. Donadio, M. Parrinello. Canonical Sampling through Velocity Rescaling. *J. Chem. Phys*. **126**, 014101–014107 (2007).

53. H. J. C. Berendsen, J. P. M. Postma, W. F. van Gunsteren, A. DiNola, J. R. Haak. Molecular Dynamics with Coupling to an External Bath. *J. Chem. Phys*. **81**, 3684–3690 (1984).

54. H. Heinz, R. A. Farmer, R. R. Naik. Accurate Simulation of Surfaces and Interfaces of Face-Centered Cubic Metals Using 12-6 and 9-6 Lennard-Jones Potentials. *J. Phys. Chem. B* **112**, 17281–17290 (2008).

55. H. Heinz, B. L. Farmer, R. B. Pandey, J. M. Slocik, S. Patnaik, R. Pachter, R. R. Naik. Nature of Molecular Interactions of Peptides with Gold, Palladium, and Pd-Au Bimetal Surfaces in Aqueous Solution. *J. Am. Chem. Soc.* **131**, 9704–9714 (2009)

56. S. K. Meena, M. Sulpizi. From Gold Nanoseeds to Nanorods: The Microscopic Origin of the Anisotropic Growth. *Angew. Chem. Int. Ed.* **55**, 11960–11964 (2016).

57. K. Momma, F. Izumi. VESTA 3 for Three-Dimensional Visualization of Crystal, Volumetric and Morphology Data. *J. Appl. Cryst*. **44**, 1272–1276 (2011).

58. J. M. Taboada, M. G. Araujo, F. Obelleiro, J. L. Rodriguez, L. Landesa. MLFMA-FFT Parallel Algorithm for the Solution of Extremely Large Problems. *Electromagnetics. Proc. IEEE*, ***101***, 350−363 (2013).

59. D. M. Solis, J. M. Taboada, L. Landesa, J. L. Rodriguez, and F. Obelleiro, Squeezing Maxwell's Equations into the Nanoscale. *Prog Electromagn Res.,***154**, 35–50 (2015).

60. P. B. Johnson, R. W. Christy, Optical Constants of the Noble Metals. *Phys. Rev. B*, **6**, 4370−4379 (1972).

61. E. D. Palik, *Handbook of Optical Constants of Solids*; (Academic Press: San Diego, 1985).

ACKNOWLEDGMENTS

Funding: L.M.L.-M. acknowledges funding from the European Research Council (ERC AdG No. 787510). G.G.-R. and J.M. thanks the Spanish MICIU for FPI (BES-2014-068972) and Juan de la Cierva-fellowships (FJCI-2015-25080). S.B., L.M.L.-M., V.K, and A.P.-T. acknowledge financial support from the European Commission under the Horizon 2020 Programme by means of the grant agreement No. 731019 (EUSMI) and the ERC Consolidator Grant No. 815128 (REALNANO). J.M.T and F.O acknowledge financial support from the Spanish MICIU (Grants TEC2017-85376-C2-1-R, TEC2017-85376-C2-2-R), as well as from the ERDF and the Galician Regional Government as part of the agreement for funding the Atlantic Research Center for Information and Communication Technologies (AtlantTIC). AG-M acknowledges financial support from the Spanish MICIU (Grant RTI2018-095844-B-I00), EGN and LGM acknowledge funds from the Spanish MICIU (Grant No. FIS2017-89361-C3-2-P), as well as the use of the Mare-Nostrum supercomputer and the technical support provided by Barcelona Supercomputing Center from the Spanish Network of Supercomputing (Grants QCM-2018-3-0039 and QCM-2019-1-0038). This work was performed under the Maria de Maeztu Units of Excellence Program from the Spanish State

Research Agency – Grant No. MDM-2017-0720. **Authors contributions:** G.G.-R., J.M. and L.M.L.-M. conceived the project. G.G.-R., J.M. and V.K. performed NP synthesis and CD experiments. A. P.-T., I.L., and S.B. carried out EM characterization and analysis. P.Ll., E.G.N. and L.G.M. executed and analyzed MD simulations. D.M.S., E.G.N. J.M.T. and F.O. carried out electromagnetic modeling of plasmonic properties of chiral NPs. G.G.-R., J.M., A.G.-M., S.B. and L.M.L.-M. wrote the manuscript with comments from all authors. L.M.L.-M. supervised the project. **Competing interests:** The authors declare no competing interests. **Data and materials availability:** All data needed to evaluate the conclusions in the paper are presented in the paper or the Supplementary Materials.

Supplementary Materials:
Materials and Methods
Figs. S1-S26
Tables S1-S6
Movies S1-S48
References (45-61)

Figures

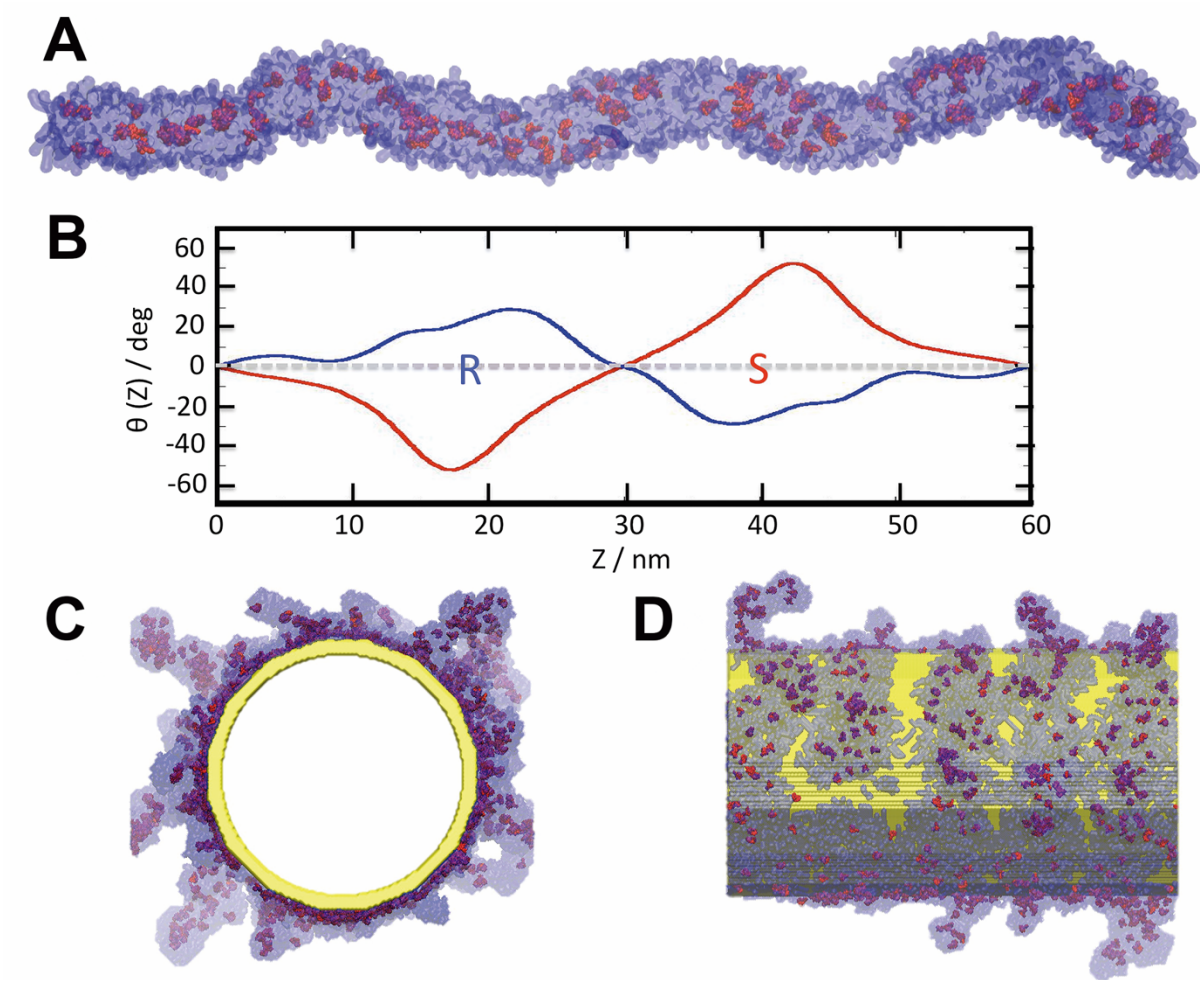

Figure 1. MD simulations of BINOL/CTAC micellar system and their assembly on gold nanorods. (A) MD Simulations for (*R*)-BINOL/CTAC in solution. The aggregation of CTA^+ (blue) in the presence of (*R*)-BINOL (red) results in chiral worm-like aggregates spanning the whole simulation box: 60 nm in length. (B) The shape of the micellar coil is described by a set of vectors along the principal micellar axis. The average angle between vectors is plotted as a function of their vertical distance for 60 nm long rod-like micelles. The presence of (*R*)- or (*S*)-co-surfactant enantiomers in the micelles leads to coiling in opposite directions, as revealed by the sign of the average angle. (C, D) MD simulations for (*R*)-BINOL /CTAC adsorbed onto a gold nanorod in axial and lateral views, respectively.

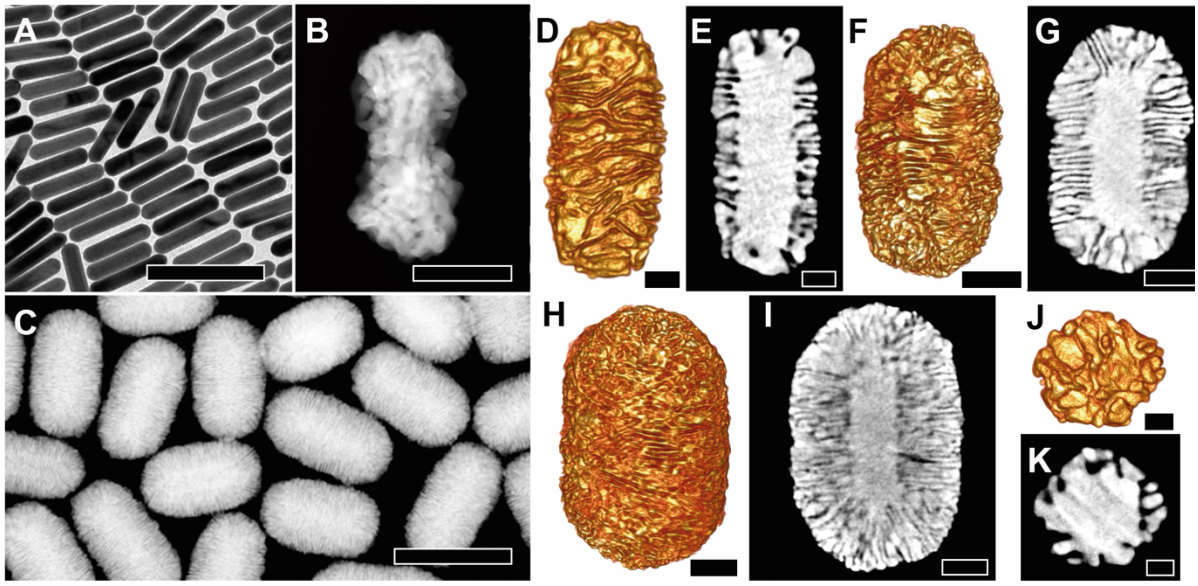

Figure 2. Growth of chiral gold nanorods in micellar systems and effects of size and shape. (A) TEM image of gold nanorods of 130 nm in length and 29 in width, used as seeds. (B) High magnification HAADF-STEM image of a chiral gold nanorod grown in (*R*)-BINOL, displaying a complex surface containing wrinkles. (C) HAADF-STEM image at low magnification of gold nanorods obtained in the presence of (*R*)-BINAMINE, displaying a complex surface containing sharp wrinkles. Scale bars: 200 nm (A,C), 100 nm (B). (D to I) Gold nanorods of 165 nm by 73 nm (D, E), 210 nm by 112 nm (F, G), and 270 nm by 175 nm (H, I) grown in (*R*)-BINAMINE/surfactant mixtures were analyzed by HAADF-STEM. Scale bars: 20 nm (D, E), 50 nm (F, G), 100 nm (H, I) and 10 nm (J, K). Tomography reconstructions (D, F and H) reveal their surface topography, whereas selected orthoslices show the growth of wrinkles from the gold nanorod seeds and the internal structure of the wrinkles network (E, G and I). (J, K) Tomography reconstruction and selected orthoslice of a nanoparticle obtained by overgrowth of a 30 nm gold nanosphere in an (*R*)-BINAMINE/surfactant mixture. Scale bar: 100 nm. Corresponding animated reconstructions are provided in Movies S1 (D), S3 (E), S7 (F), S9 (G), S18 (H), S20 (I), S43 (J) and S45 (K).

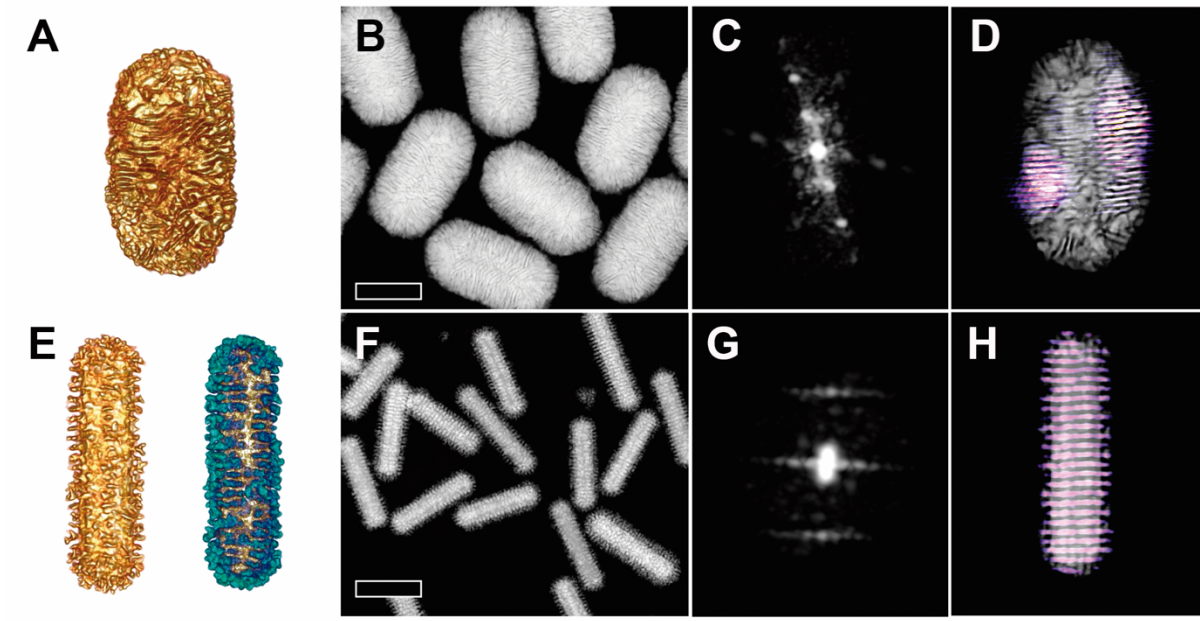

Figure 3. Qualitative analysis of chiral features. (A) Tomography reconstruction of a gold nanorod grown in (*R*)-BINAMINE/surfactant mixture (see also Movie S7). (B) Low resolution HAADF-STEM image of chiral gold nanorods obtained in the presence of (*R*)-BINAMINE. Scale bar: 100 nm. (C) 3D-FFT from which the inverse FFT was computed after segmentation (see also Movie S10). (D) The inverse FFT (see also Movie S12) shows the areas of the particle with chiral features overlapped with the projection of the tomography, indicating a right-handed angle. (E) Tomography reconstruction in HAADF-STEM (left) and EDX (right) modes, of an Au@Pt nanorod grown in (*R*)-BINOL/surfactant mixture (see also Movies S24 and S25). (F) HAADF-STEM image at low magnification of Au@Pt nanorods. Scale bar: 100 nm. (G) 3D-FFT from which the inverse FFT was computed after segmentation (see also Movies S28 and S29). (H) The inverse FFT (see also Movie S30) shows the areas of the particle with chiral features overlapped with the projection of the tomography, indicating a right-handed lower angle.

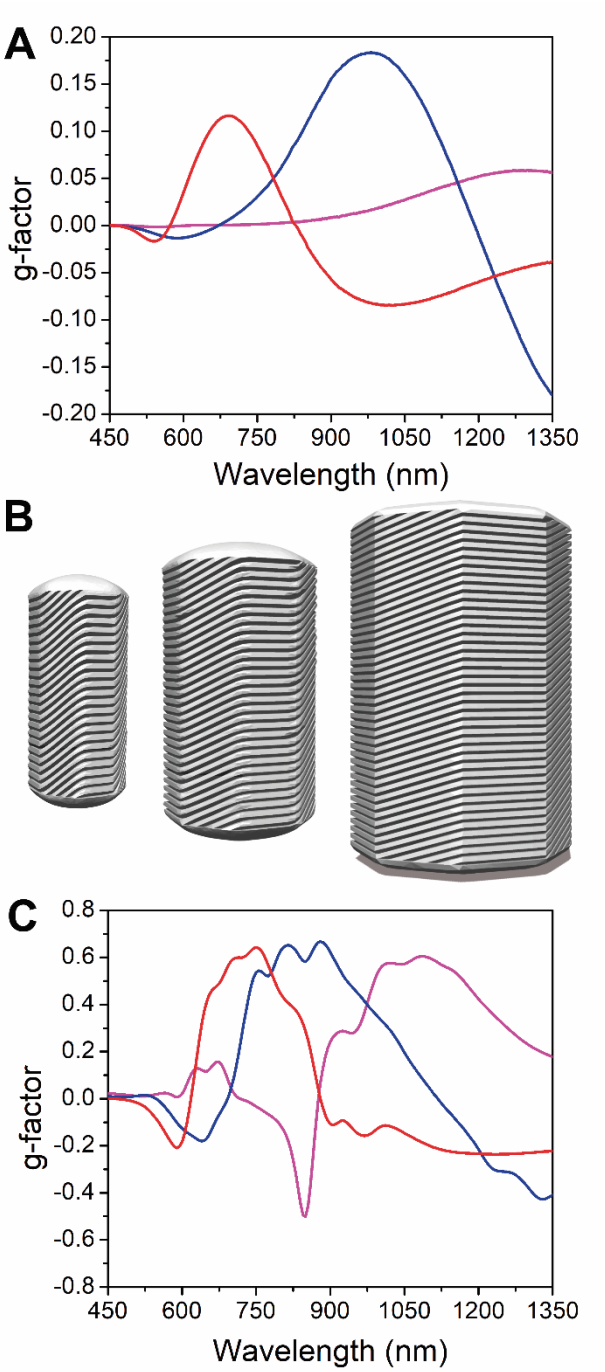

Figure 4. Effect of nanorod dimensions on the chiral plasmonic activity. (A) Spectral evolution of the anisotropy factor for chiral nanorods with increasing particle size: 165 nm by 73 nm (red), 210 nm by 112 nm (blue) and 270 nm by 175 nm (magenta). (B) Models of chiral gold nanorods used to simulate the chiral plasmonic properties (from left to right: 165 nm by 73 nm, 210 nm by 112 nm and 270 nm by 175 nm). (C) Calculated anisotropy factor spectra (from left to right in C: red, blue, and magenta).

Supplementary Materials for

Micelle-Directed Chiral Seeded-Growth on Anisotropic Gold Nanocrystals

Guillermo González-Rubio, Jesús Mosquera, Vished Kumar, Adrián Pedrazo-Tardajos, Pablo Llombart, Diego M. Solís, Ivan Lobato, Eva G. Noya, Andrés Guerrero-Martínez, José M. Taboada, Fernando Obelleiro, Luis G. MacDowell, Sara Bals*,

Luis M. Liz-Marzán*

correspondence to: sara.bals@uantwerpen.be; llizmarzan@cicbiomagune.es

This PDF file includes:

Other Suplementary Materials for this manuscript include the following:

Materials and Methods

Characterization Techniques

Transmission electron microscopy. TEM images were obtained using a JEOL JEM-2100 transmission electron microscope operating at an acceleration voltage of 200 kV. All samples were centrifuged to remove the excess of surfactant (final [surfactant] =1 mM) prior to blotting on carbon-coated 400 square mesh copper grids.

Electron tomography. Tomography tilt series were acquired by tilting the samples using a Fischione 2020 holder over ±72° with a tilt increment of 3°. Hereby, the individual HAADF-STEM images were acquired using an aberration-corrected 'cubed' FEI-Titan electron microscope operated at 300 kV with a camera length of 58 mm. To eliminate different image distortions, we applied non-rigid registration methods in combination with a convolutional neural network (CNN) (*45*). This protocol uses multiple successive images as an input, in this case 10 frames of 1kx1k with a scan time of 0.5 s for each frame consecutively. Undistorted images were aligned with respect to each other by using a phase correlation, which was also used to determine the shift and the angle of the rotation axis. 3D reconstruction was performed by a novel approach consisting of iterating between 50 SIRT cycles and application of constraints in the real and Fourier space (*45*). After applying a bandwidth limit to the FFT, the result is transformed to real space and a threshold is applied to the intensity of the 3D volume. Next, the SIRT cycles are repeated. In this manner, a high quality 3D reconstruction with diminished missing wedge is obtained. This resulted in a data set in reciprocal space, which was then segmented to reduce noise and used as an input for inverse FFT. In this manner, we were able to connect the frequencies observed in reciprocal space to the chiral features in real space.

EDX measurements were recorded using an Osiris microscope, operated at 200 kV. Acquisition of tilt series for tomography was done by collecting EDX data over a range of ±70° with a tilt increment of 10°. In order to align the series, we used a simultaneously acquired HAADF-STEM series obtained over ±72° with a tilt increment of 3° (*46*). The 3D reconstruction was performed by the Total Variation Minimization algorithm using 20 iterations (*47*).

UV/Vis/NIR spectroscopy. All measurements were carried out using a Cary 5000 UV-Vis-NIR spectrometer at 298 K and quartz cuvettes with 0.2 cm optical path length.

Circular Dichroism spectroscopy. Circular dichroism spectra were acquired using a JASCO J-1500 CD spectrometer. All measurements were performed in CD/DC mode. CD spectra were acquired in two steps, from 400 nm-900 nm and from 800 nm-1600 nm. Both spectra were then integrated using ¨Spectra Concatenation¨ software from JASCO to obtain an integrated CD spectrum from 400-1600 nm.

Synthesis Details

Materials. All starting materials were obtained from commercial suppliers and used without further purification: 1-decanol (*n*-decanol, 98%), hexadecyltrimethylammonium bromide (CTAB, ≥99%), *(R)*-(+)-1,1′-Bi(2-naphthol) ((*R*)-BINOL, 99%), (*R*)-(+)-1,1′-binaphthyl-2,2′-diamine ((*R*)-BINAMINE, 99%), (*S*)-(-)-1,1′-binaphthyl-2,2′-diamine ((*S*)-BINAMINE, 99%), (*R*)-(+)-2′-Amino-1,1′-binaphthalen-2-ol (97%), sodium hypochlorite (available chlorine 10−15%), hydrogen tetrachloroaurate trihydrate ($HAuCl_4 \cdot 3H_2O$, ≥99.9%), silver nitrate ($AgNO_3$, ≥99.0%), potassium tetrachloroplatinate (K_2PtCl_4, 98%), L-ascorbic acid (≥99%), hydrochloric acid (37%) and sodium borohydride ($NaBH_4$, 99%) were purchased from Aldrich. Hexadecyltrimethylammonium chloride (CTAC, 99%) was purchased from ACROS Organics. Nanopure water (resistivity 18.2 MΩ·cm at 25 °C) was used in all experiments.

Synthesis of gold nanorods. Gold nanorods were prepared using the seeded growth method with some modifications, as previously described by González-Rubio et al (*27*):

- *CTAB/n-decanol solution*: 9.111 g of CTAB (50 mM) and 1.068 g (13.5 mM for 1–2 nm and small anisotropic seeds) or 870.5 mg (11 mM for gold nanorods synthesis) of *n*-decanol were weighed directly in a 500 mL Erlenmeyer flask. 500 mL of water was added and the mixture stirred for 3h at 35 °C until complete dissolution of CTAB and *n*-decanol. The solution was stable while the temperature was kept above 16 °C. Importantly, freshly prepared solutions were used for the synthesis of both types of seed.
- *Synthesis of 1–2 nm gold seeds*. 20 mL of a CTAB (50 mM) / *n*-decanol (13.5 mM) mixed solution was placed in a 50 mL glass beaker at 25–27 °C and then 200 µL of $HAuCl_4$ (0.05 M) and 100 µL of ascorbic acid (0.1 M) were added. After 1–2 min, 800 µL of a freshly prepared 0.02 M $NaBH_4$ solution was injected under vigorous stirring into the colorless solution (1000 rpm using a PTFE plain magnetic stirring bar: 30 × 6 mm, at 25–27 °C). A brownish-yellow solution was obtained, which was then aged for at least 60 min at 25–27 °C prior to use.
- *Synthesis of small anisotropic seeds (21 nm long, 7.5 nm wide)***.** In a 500 mL Erlenmeyer flask, 3.0 mL of $HAuCl_4$ (0.05 M), 2.4 mL of $AgNO_3$ (0.01 M), 21.0 mL of HCl (1 M), and 3.9 mL of ascorbic acid (0.1 M) were added to 300 mL of a CTAB (50 mM) / *n*-decanol (13.5 mM) mixed solution at 25 °C. Under stirring, 18 mL of the seed solution was then added. After 4 h at 25 °C, the mixture changed from colorless to grey and finally dark brownish grey, indicating the formation of small anisotropic nanocrystals with LSPR at 725–730 nm. The obtained small anisotropic seeds were centrifuged at 14000–15000 rpm for 45–60 min. The supernatant was discarded and the precipitate was collected and re-dispersed in 30 mL of a CTAB (10 mM) solution. The concentrated gold nanorod colloid was centrifuged again at 14000–15000 rpm for 45–60 min and the precipitated small gold nanorods were redispersed in 30 mL of a CTAB (10 mM) solution. This step was repeated one more time. Finally, the gold concentration was fixed to 4.65 mM (abs at 400nm: 1, optical path: 0.1 cm) by adjusting the volume of CTAB (10mM) solution added to redisperse the nanoparticles precipitated in the last centrifugation step.
- *Gold nanorods of different dimensions:* In a 250 mL Erlenmeyer flask, 100 mL of n-decanol (11 mM) / CTAB (50 mM) mixed solution, 1.0 mL of $HAuCl_4$ (0.05 M) and 1.5 mL of $AgNO_3$ (0.01 M) were mixed under magnetic stirring. To control the nanorods dimensions, the concentration of anisotropic seed, temperature and HCl were varied (table S1). Prior to the addition of seeds, 800 µL of ascorbic acid (100 mM) was added. The temperature of the solution was controlled using a Julabo F-25 refrigerator/heating circulator. The mixture was kept undisturbed overnight at 16 °C for growth of AuNR with LSPR at 930 and 1220 nm, and at 25 °C for AuNR with LSPR at 762 nm. Finally, the obtained nanorods were centrifuged at 3000-6000 rpm (10-15 min) and redispersed in 10 mL of CTAC (10 mM). This step was repeated twice to remove excess CTAB.

Synthesis of gold nanospheres: Gold nanospheres were prepared using the seeded growth method with some modifications, as previously described by Hanske et al (*48*).

- *Synthesis of 1–2 nm gold seeds*. 5 mL of CTAC (0.1 M) was placed in a 15 mL glass vial and 50 µL of $HAuCl_4$ (0.05 M) was added, followed by fast injection of 200 µL of freshly prepared $NaBH_4$ (0.02 M; 7.6 mg/10 mL), under vigorous stirring. The mixture was aged for 3 min and diluted 10-fold with CTAC (100 mM).
- *10 nm seeds*. 10 mL of CTAC (25 mM) was placed in a 15 mL glass vial and 900 µL of seed solution was added, followed by 40 µL of ascorbic acid (0.1 M). Then, 50 µL

of $HAuCl_4$ (0.05 M) was injected under vigorous stirring. After 10 min, the resulting gold nanospheres presented an LSPR band centered at 520 nm.

- *30 nm gold nanospheres.* 3125 µL of 10 nm gold nanospheres suspension and 1000 µL of ascorbic acid (0.1 M) were added to 250 mL of CTAC (25 mM). Subsequently, 1250 µL of $HAuCl_4$ (0.05 M) was added under vigorous stirring. The mixture was left undisturbed at room temperature for at least 1 h. At this stage, the obtained nanoparticles were highly faceted and presented LSPRs located at ca. 543 nm. To reduce the surface roughness, oxidative etching of the facets was carried out. First, 250 µL of a dilute sodium hypochlorite solution (1 to 1.5 wt % of available chlorine) was added under rapid stirring at 30 ºC. Note that sodium hypochlorite degrades over time and therefore larger volumes may be needed when using aged stock solutions. After 5-10 min, a 10-15 nm blueshift of the LSPR band was observed due to partial oxidation of the facets. To complete the oxidation, $HAuCl_4$ was used as oxidizing agent: between 75 and 125 µL of $HAuCl_4$ (50 mM) was added under fast stirring. The mixture was left under moderate stirring at 30 ºC until the absorbance at 400 nm decreased by 10-20% (ca. 30 min) and the band of Au (III)-CTAC (at 226 and 325 nm) almost disappeared. Once oxidation was completed, the resulting 30 nm gold nanospheres were immediately centrifuged to remove Au (I) produced during oxidative etching and thereby avoid re-deposition on the nanoparticles.

The quality of CTAC has a great influence on the synthesis and the size dispersity of the obtained nanospheres. It is recommended to check the size dispersity of the obtained faceted nanoparticles prior the oxidative etching. If a high size polydispersity is observed, a new CTAC batch or higher purity CTAC are required.

Growth of chiral gold nanoparticles:

- *Preparation of chiral co-surfactant/CTAC solution*: In a 50 mL glass vial, a certain amount of chiral co-surfactant (see table S2) and 1600 mg of CTAC were weighed. Then, 50 mL of water was added and the mixture was heated at 60 ºC for 3 hours (or until complete dissolution of the co-surfactant), under stirring. The solution was then allowed to cool down to room temperature before further use. The concentration of CTAC and co-surfactant were fixed to 100 mM and 2.5 mM, respectively.
- *Washing of the Nanoparticles.* We observed that the presence of silver traces (in gold nanorods synthesis) or impurities in the reactants (e.g., alkyl amines or iodide in CTAB) used during the synthesis of the nanoparticles had a negative effect on the growth of chiral features. For this reason, 2 mL solution of gold nanoparticles ([Au(0)] =10 mM) was washed at least 2 times with 2 mL of 10 mM CTAC (purity 99%), followed by two more washes with chiral co-surfactant/CTAC solution. Finally, the particles were redispersed in the chiral co-surfactant/CTAC solution ([Au(0)] =10 mM) and aged overnight prior to use. In the case of BINAMINE, we observed that using a slightly supersaturated solution (maximum CTAC:BINAMINE ratio of 40, excess of 0.1- 0.2 mg/mL) provided better reproducibility and higher quality chiral nanoparticles.
- *Preparation of chiral gold nanoparticles:* In a 2 mL Eppendorf tube, 10 µL of Au(III) solution (50 mM) was added to a mixture of 600 µL of milli-Q water and 200 µL of chiral co-surfactant/CTAC solution. This solution was shaken and allowed to rest at room temperature for five minutes to allow complexation of Au(III) with CTAC. When BINAMINE was used as co-surfactant, the mixture changed from yellow to brown during incubation. Different volumes of nanoparticles colloid (table S3) were introduced in the above solution followed by fast addition of 200 µL of ascorbic acid

(0.8 M). The solution was shaken vigorously and then allowed to rest for 10–15 minutes. The solution was then centrifuged and re-dispersed in 1 mL of cysteine (2 mM) / CTAC (10 mM) stock solution.

Growth of chiral platinum shells on gold nanorods: In a 2 mL Eppendorf tube, 10 μL of K_2PtCl_4 solution (50 mM) was added to a mixture of 600 μL of milli-Q water and 200 μL of BINOL/CTAC solution. This solution was shaken and allowed to rest at 30 ºC in a water bath for 10-15 minutes. A small volume of gold nanorod dispersion (see values in table S3) was then introduced in the above solution, followed by fast addition of 200 μL of ascorbic acid (0.8 M). The solution was shaken vigorously and then kept undisturbed overnight in a water bath at 30 ºC for complete growth of platinum around gold nanorods. The solution was subsequently centrifuged and redispersed in a CTAC (10 mM) stock solution.

Molecular Dynamics simulation of BINOL and BINAMINE in CTAC solutions

Force field: Molecular simulations were performed using GROMACS. All bonded interactions, as well as Lennard-Jones interactions for CTAC and the selected enantiomers were described using the GROMOS-53a6 force field. Crossed interactions between unlike united atom groups were computed using the geometric combination rules from GROMACS (see table S4). The partial charge assignment for the CTA^+ was obtained from DFT calculations previously described (*49*). The charge assignment for BINOL and BINAMINE was obtained using the Automated Topology Builder (ATB) (*50*).

Free micelles in solution: The initial configuration was obtained by equilibration of SPC water at 298 K and 1 bar in an orthorhombic simulation box of dimensions Lx, Ly and Lz. Next, a cylindrical cavity with 3 nm radius was carved in the center of the simulation box along the z axis. CTA^+ and BINOL enantiomers were placed randomly inside the cavity using PACKMOL (*51*). The system was neutralized by inserting Cl^- counterions randomly within the simulation box. Further stabilization was achieved by random insertion of added NaCl (see table S5 for details on simulation box dimensions and number of molecules). The configuration was relaxed in three stages. First, water molecules were kept at fixed position, and a steep descent minimization of the micelle was performed until the maximum forces converged below 1000 kJ mol^{-1} nm^{-1}. The constraint system was further relaxed in an NVT simulation performed over 2 ns. These preliminary stages were required to stabilize the micelle. Finally, the full unconstrained system was simulated in the NPT ensemble at 1 bar. We used the velocity-rescale thermostat (*52*) and the Berendsen barostat (*53*) with a 2 ps relaxation time to control temperature and pressure at desired values, respectively. The NPT simulations were equilibrated over 15 ns, and production runs were performed over the next 30 ns. Similar runs were performed with BINOL replaced by BINAMINE. Equations of motion were integrated using the velocity-verlet algorithm, with a time step of 3 fs. Configurations were saved for further analysis every 75 ps. Coulomb interactions were computed using Particle Mesh Ewald with metallic boundary conditions and a real space cutoff of 1.2 nm. The simulation box was set with a base Lx=Ly of approximately 10 nm, and height Lz of approximately 10, 30 and 60 nm, as described in table S5.

Density profiles: To probe the shape of micellar aggregates we analyzed density profiles of CTA^+ heads for x-y projection and CTA^+ molecules for x-z projection. The simulation box typically contained a large micellar cluster, together with some additional small satellite aggregates and free surfactant molecules. We performed a cluster analysis to identify the CTA^+ molecules belonging to the largest cluster. We assumed that all atoms at a distance below 4.2 Å belong to the same cluster. Once the cluster was located, we sought a local micellar reference frame by calculating the principal axes of inertia. Density contour plots were obtained by projecting the density onto planes perpendicular to a given axis (fig. S1).

Helicity: In order to measure the helicity of the cylindrical micelles, we analyzed instantaneous configurations of the simulation box. For a given configuration, we divided the full cylinder into small cylindrical sections of 1 Å in height. The center of mass, $\mathbf{r}_{cm}(i)$ of each section i, was calculated from the carbon atoms of CTA^+. With the set of centers of mass for all sections, we calculated the instantaneous center of mass of the full micelle, $\mathbf{R}_{cm}$, which serves to locate the main cylinder axis parallel to z. The deviation of section i from the micellar axis was calculated as $\mathbf{d}(i) = \mathbf{r}_{cm}(i) - \mathbf{R}_{cm}$. From the set of vectors $\mathbf{d}(i)$ we calculate $\theta(j\text{-}i)$ as the angle formed between vectors $\mathbf{d}(i)$ and $\mathbf{d}(j)$ a vertical distance z=j-i apart. In the absence of chirality, average angles $\theta(j\text{-}i)$ vanished for all j, since d(j) is as likely to be rotated clockwise as counterclockwise, with respect to d(i) and the angles are measured in the interval $[\pi,-\pi]$. A propensity for helical chirality in the micelle is manifested by finite average angles that are sinusoidally correlated as z increases (Fig. S2).

Micelles on gold nanorods: After the study of micelle stability in solution, we considered the adsorption of CTAC and BINOL on a 52.17 nm long gold nanorod. To model the nanorod surface, we employed a non-polarizable Lennard-Jones (L-J) potential for gold, as previously described by Heinz and co-workers. (*54*). All investigations were carried out at optimal thermodynamic conditions for this model (298 K, 1 bar). Thereby, the surface tension of gold and its interaction with water and surfactants can be remarkably well reproduced, while lesser computational resources were required (compared to polarizable L-J potentials) (*55*, *56*). In order to model the nanorod, we replicated a single gold unit cell in space group Fm3 (a=4.1734 Å) on the x-y plane using the program VESTA (*57*). The square array of unit cells was then cut over the [100], [110] and [250] planes about a circle of radius 17.94 nm. Since the gold nanorod was simulated with frozen atomic positions, we carved out the rod, eliminating all gold atoms inside a circle of radius 16.69 nm (see fig. S3 and table S6), to save computational cost. Once a unit cell height circular section of the rod was obtained, we replicated it 25 times in the z direction and further assumed periodic boundary conditions in all three directions of space. BINOL and CTAC were then added randomly about the nanorod in vacuo, and an NVT simulation at 298 K was performed over 2 ns. After adsorption of BINOL and CTAC, the simulation box was hydrated placing water molecules randomly. The resulting configuration was minimized with a steep descent method until the maximum pair force was below 1000 kJ/(mol nm). The simulation was then performed over 60 ns in the same conditions as described above for micelles in solution.

Electromagnetic Modeling

Simulations of the optical properties of chiral gold nanorods were carried out using the M^3 solver, which implements a full-wave frequency-domain methodology based on boundary-element parametrizations (surface integral equation-method of moments, SIE-MoM) (*40–42*, *58, 59*), thereby drastically reducing the resulting algebraic problem size if compared with conventional volumetric approaches. By applying Love's equivalence theorem, the metallic (plasmonic) nanorods can be substituted by equivalent surface electric and magnetic currents placed at the surface boundaries and radiating in unbounded media according to the Stratton-Chu expressions. Only the material boundaries (i.e., two dimensional surfaces) must be parametrized, on which the boundary conditions for the electric and magnetic fields are enforced in a variational sense with the help of functionals (specifically, we are applying the Galerkin formulation). No absorbing boundary conditions are required to close the problem. This methodology offers great accuracy for solving unbounded scattering problems, particularly when dealing with resonant plasmonic response, as the singular behavior of fields is analytically handled by the Green's function and its derivatives. The latter was especially relevant for the optical characterization of chiral nanorods in this work. This was a challenging task owing to the intricate network of oriented sharp wrinkles covering the rods

surface, whose electromagnetic response ought to be accurately handled, as it was found responsible for their chiral properties. Gold was described through its frequency-dependent complex permittivity, obtained from optical measurements (*60*, *61*). All simulations were carried out on a workstation with four 48-core Intel(R) Xeon(R) Gold 6252 CPU processors at 2.10 GHz and 3 TB RAM.

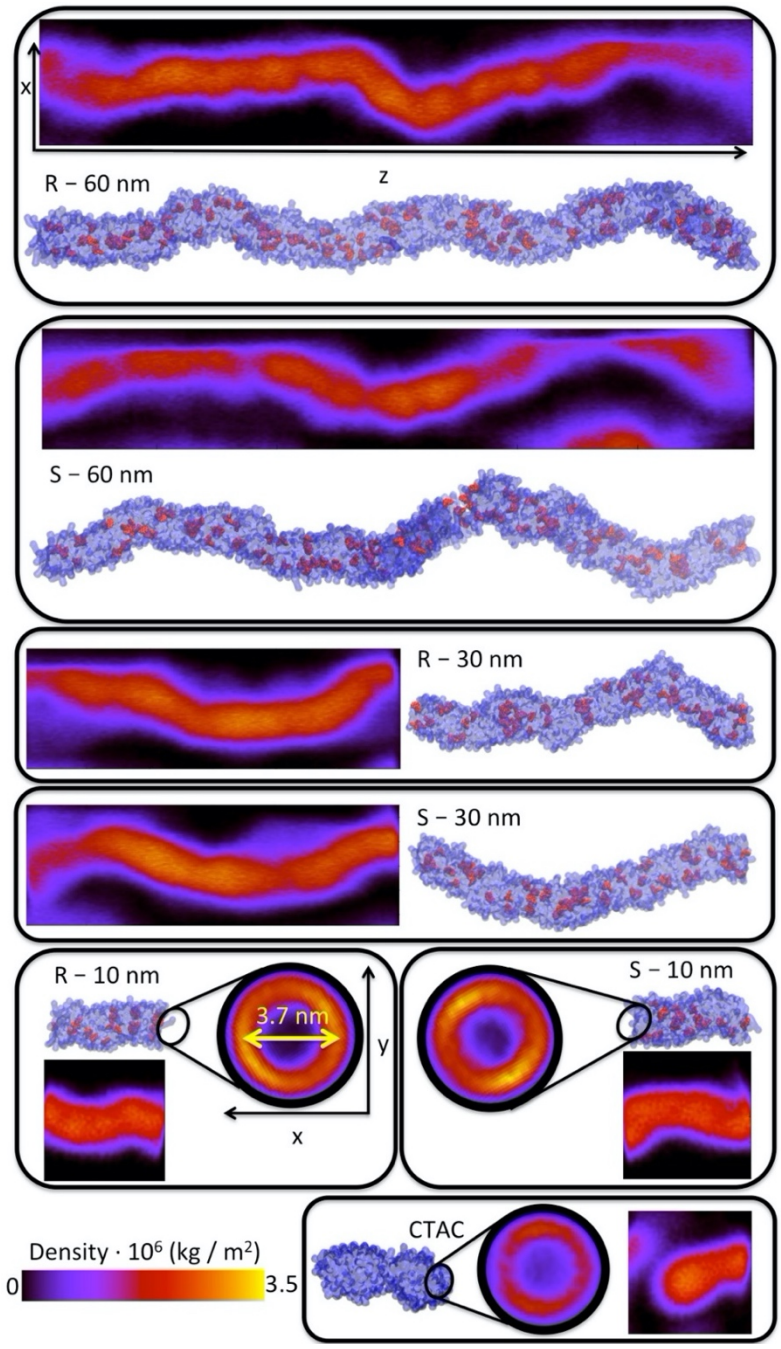

Fig. S1.

Selected snapshots obtained for simulated micelles in solution. CTA^+ is labelled in blue, BINOL molecules are labelled in red. For simulations with Lz equal to 60 nm and 30 nm, a density contour map of CTA^+ is shown, projected onto a plane containing the z axis. For simulations with Lz=10 nm, the density of CTA^+ head groups (CH_2-N-$(CH_3)_3$) is projected on a plane perpendicular to the z axis (high densities correspond to yellow/orange color). The diameter of the fiber was estimated from these profiles as 3.7 nm. In the absence of BINOL, worm-like micelles are destabilized into smaller aggregates.

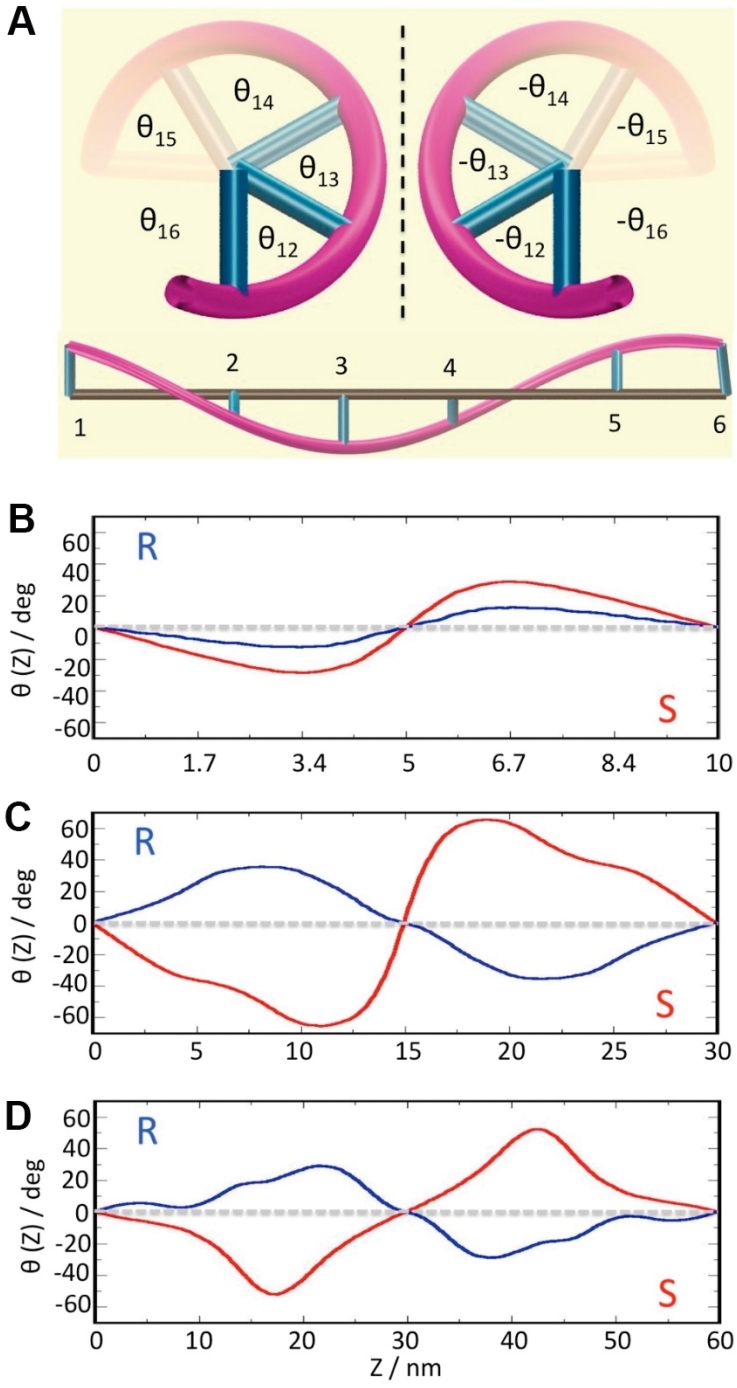

Fig. S2

(A) Clockwise and counterclockwise orientations with respect to the distance along helical axis reflect opposites angles. (B-D) Plots of the order parameter for different sizes of the simulated system: 10 nm (B), 30 nm (C) and 60 nm (D). In the case of 10 nm the helicity can be affected by the low dimension of the z-axis, not properly differentiating the sign of the helicity between R and S enantiomers.

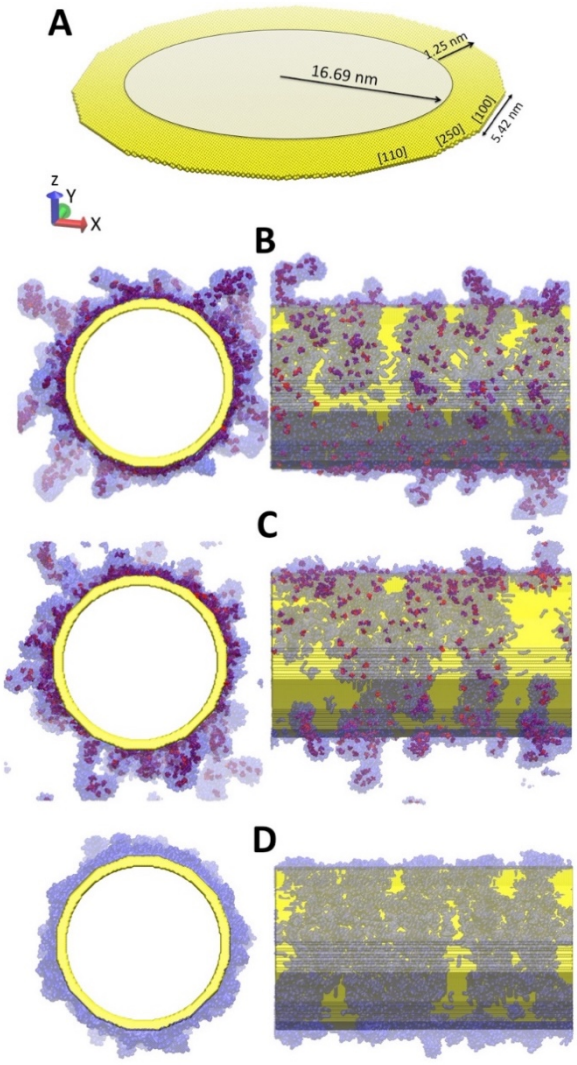

Fig. S3

(A) Elementary unit section used to replicate a gold nanorod in the z direction. (B-D) Snapshots of MD simulations projected on planes perpendicular and parallel to the rod axis. Gold atom density is shown in yellow; isosurface of CTA^+ density is shown in blue. Shown in red are BINOL molecules solvated by CTA^+. (B-C) Nanorod covered by CTA^+ containing (*R*)-BINOL (B) and (*S*)-BINOL (C). D) Nanorod covered by CTA^+ only.

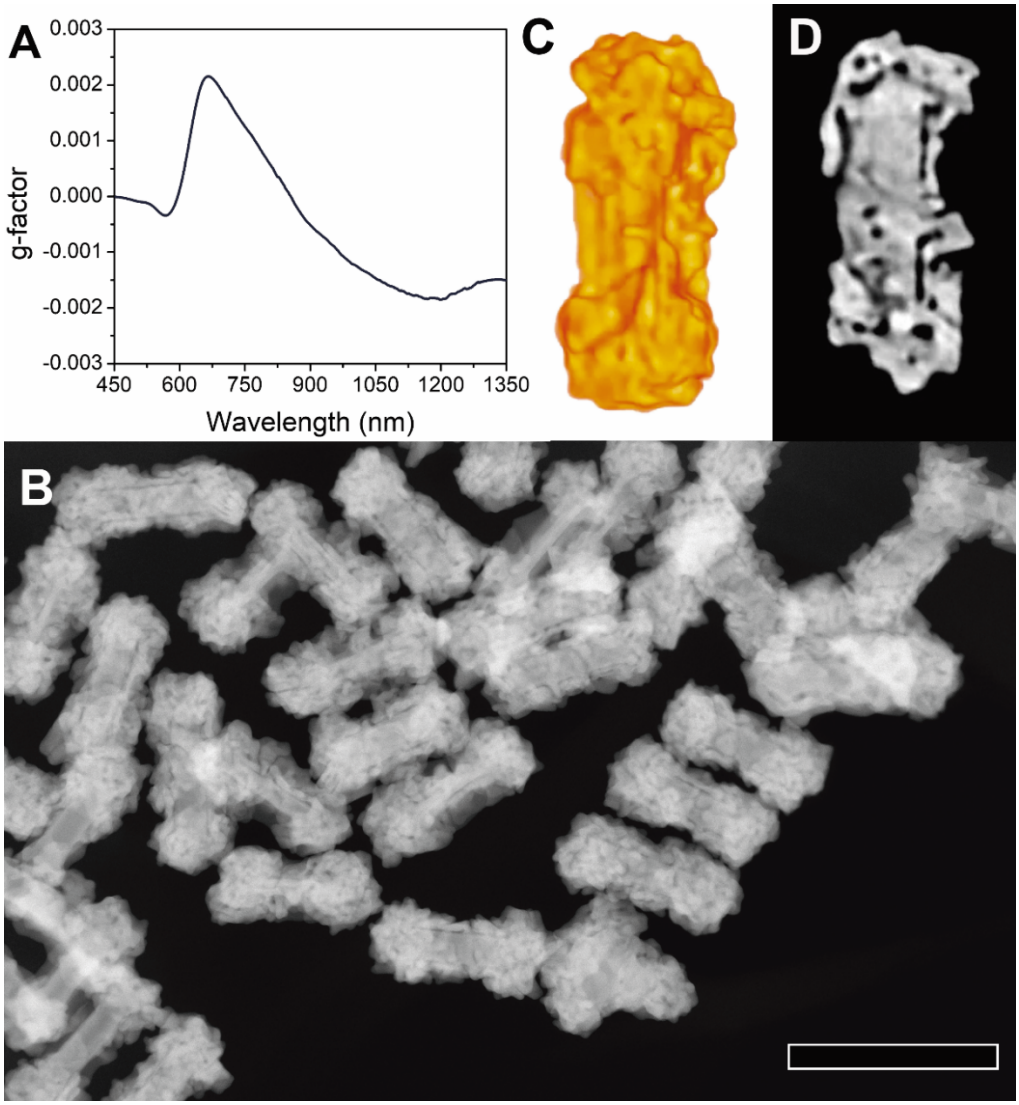

Fig. S4

Chiral gold nanorods prepared in (*R*)-BINOL/CTAC system. Dissymmetry factor spectrum (A), low magnification HAADF-STEM image (B), and tomography reconstruction (C,D) of chiral gold nanorods obtained in an (*R*)-BINOL/CTAC system at 0.16 M of ascorbic acid: the 3D visualization of the electron tomography reconstruction (C) and orthoslices through the reconstruction (D) enable investigation of the surface and 3D morphology. Scale bar in C: 200 nm.

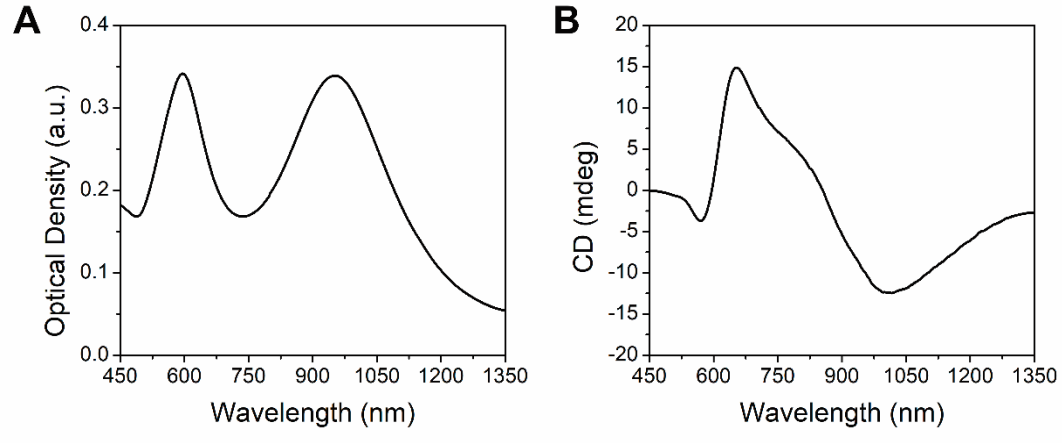

Fig. S5

UV-vis-NIR (A) and CD (B) spectra of chiral gold nanorods prepared in (*R*)-BINOL/CTAC system.

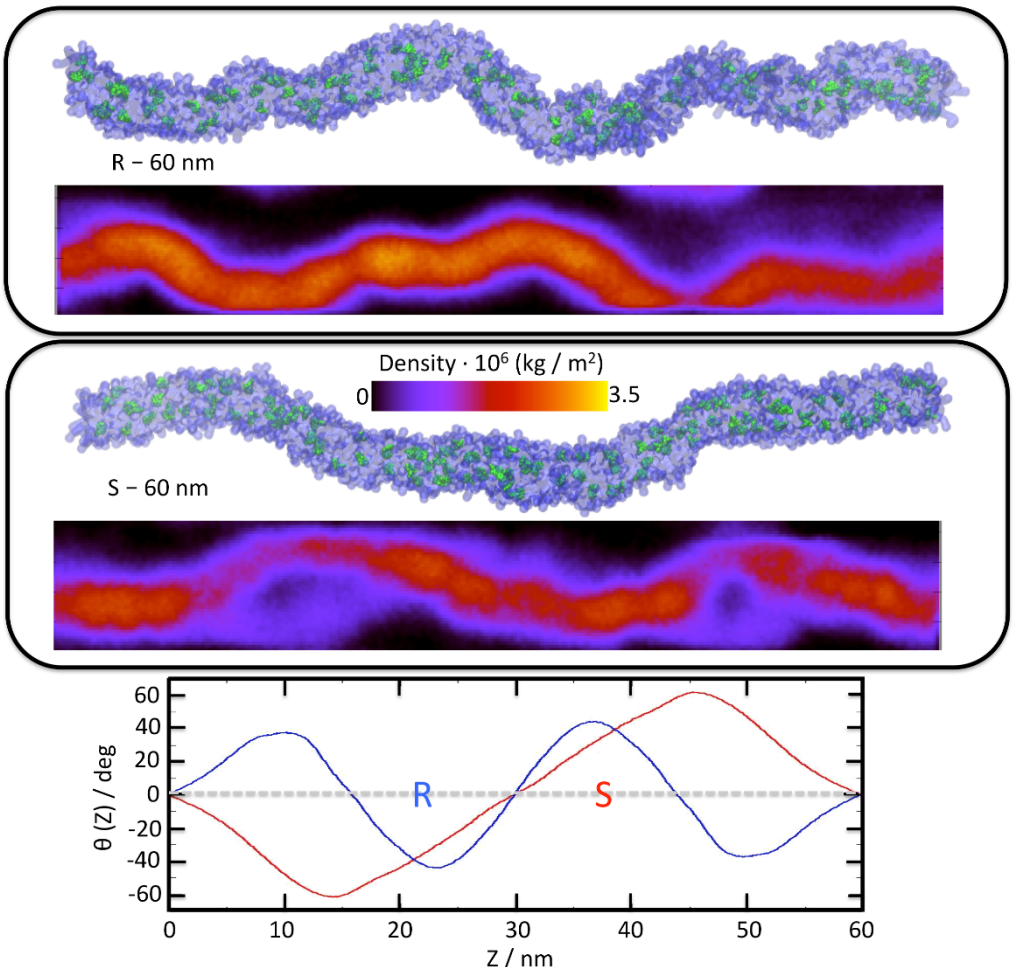

Fig. S6

Selected snapshots obtained for simulated BINAMINE/CTAC micelles in solution. CTA^+ is labelled in blue, BINAMINE molecules are labelled in green. For simulations with Lz equal to 60 nm, a density contour map of CTA^+ is shown, projected onto a plane containing the z axis (high densities correspond to yellow/orange color). The diameter of the fiber was estimated from these profiles as 3.7 nm.

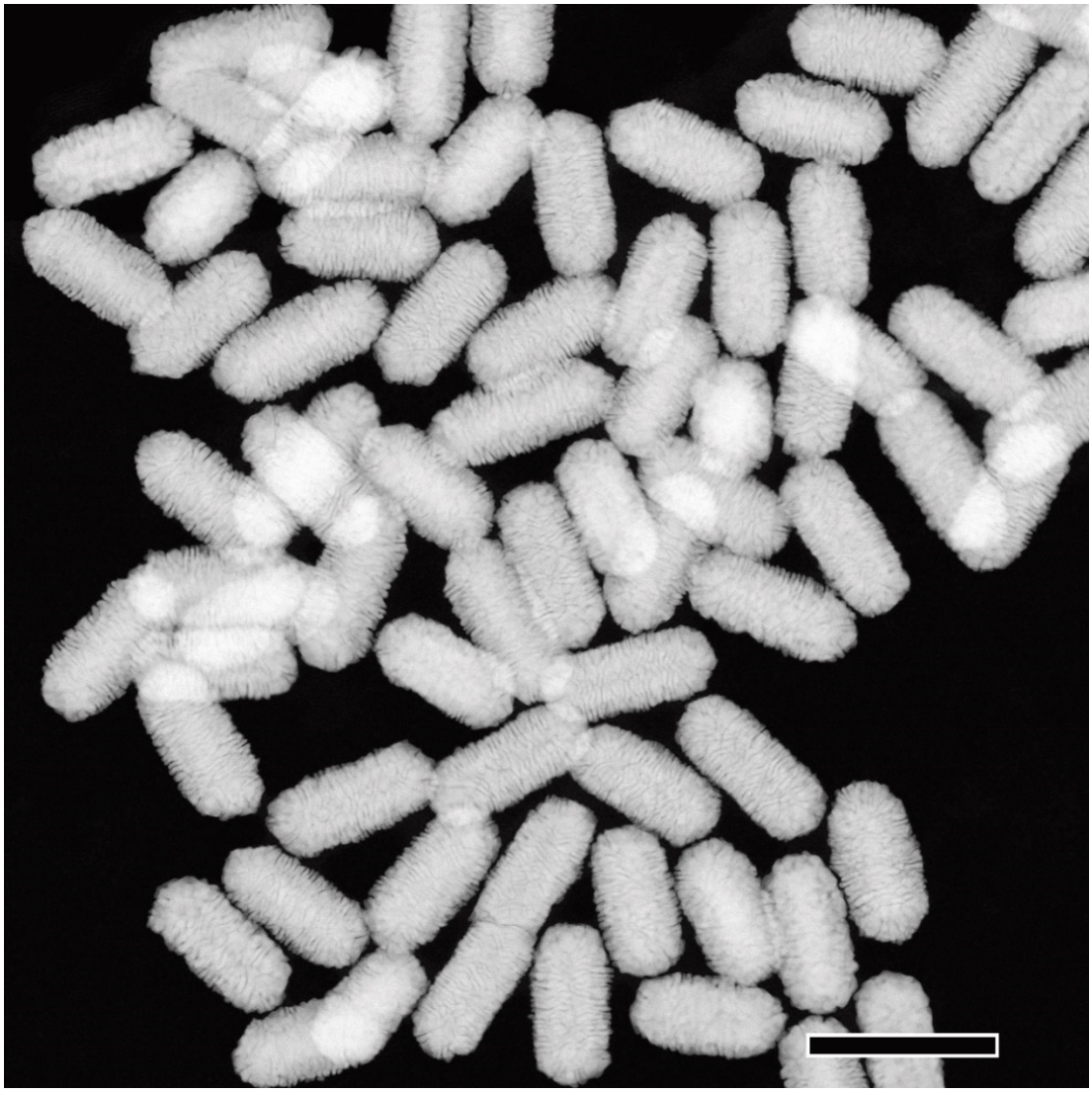

Fig. S7
Low magnification HAADF-STEM image of chiral gold nanorods (165 nm long; 73 nm wide) synthesized in (*R*)-BINAMINE/CTAC. Scale bar: 200 nm.

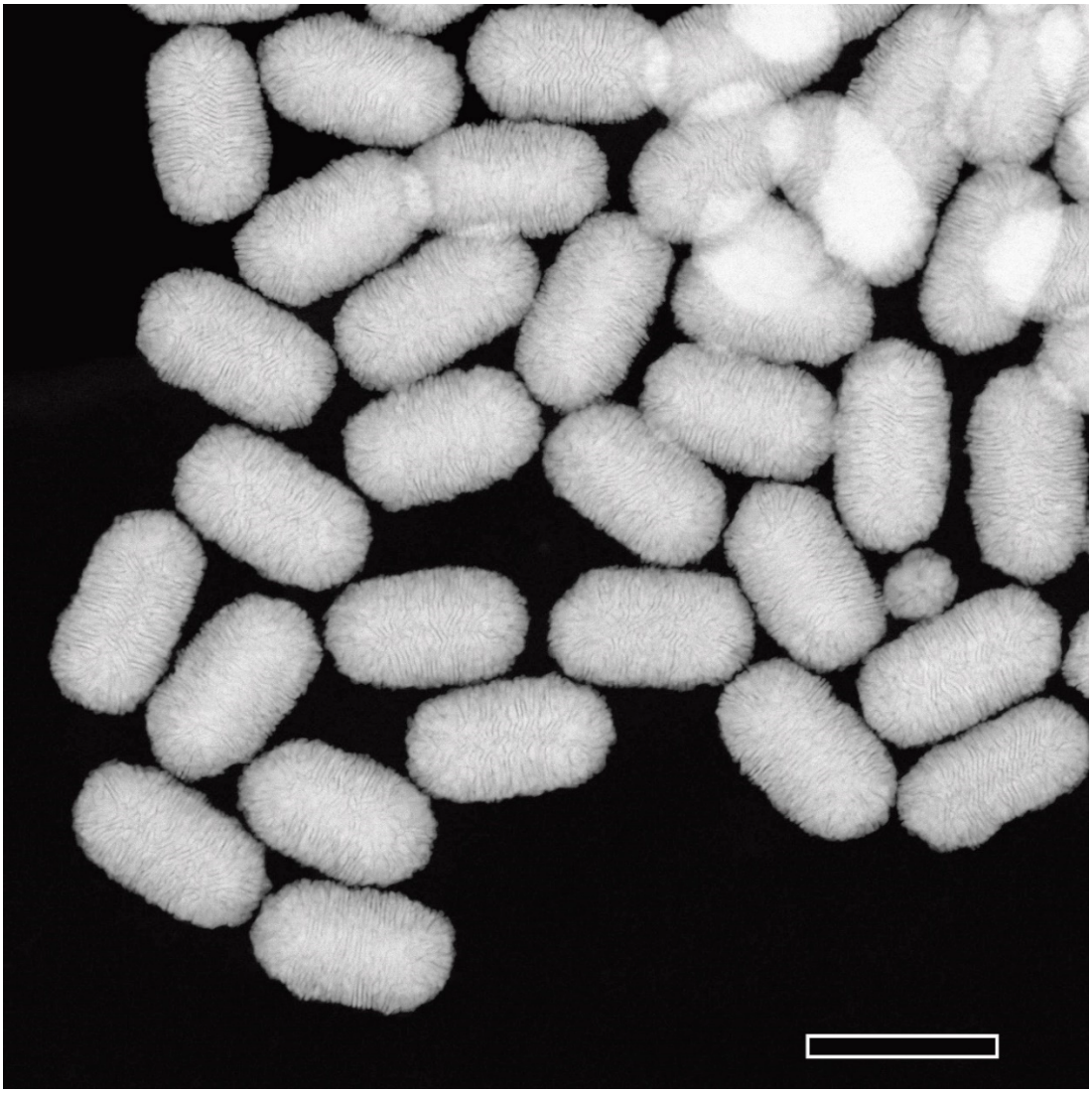

Fig. S8

Low magnification HAADF-STEM image of chiral gold nanorods (210 nm long; 112 nm wide) synthesized in (*R*)-BINAMINE/CTAC. Scale bar: 200 nm.

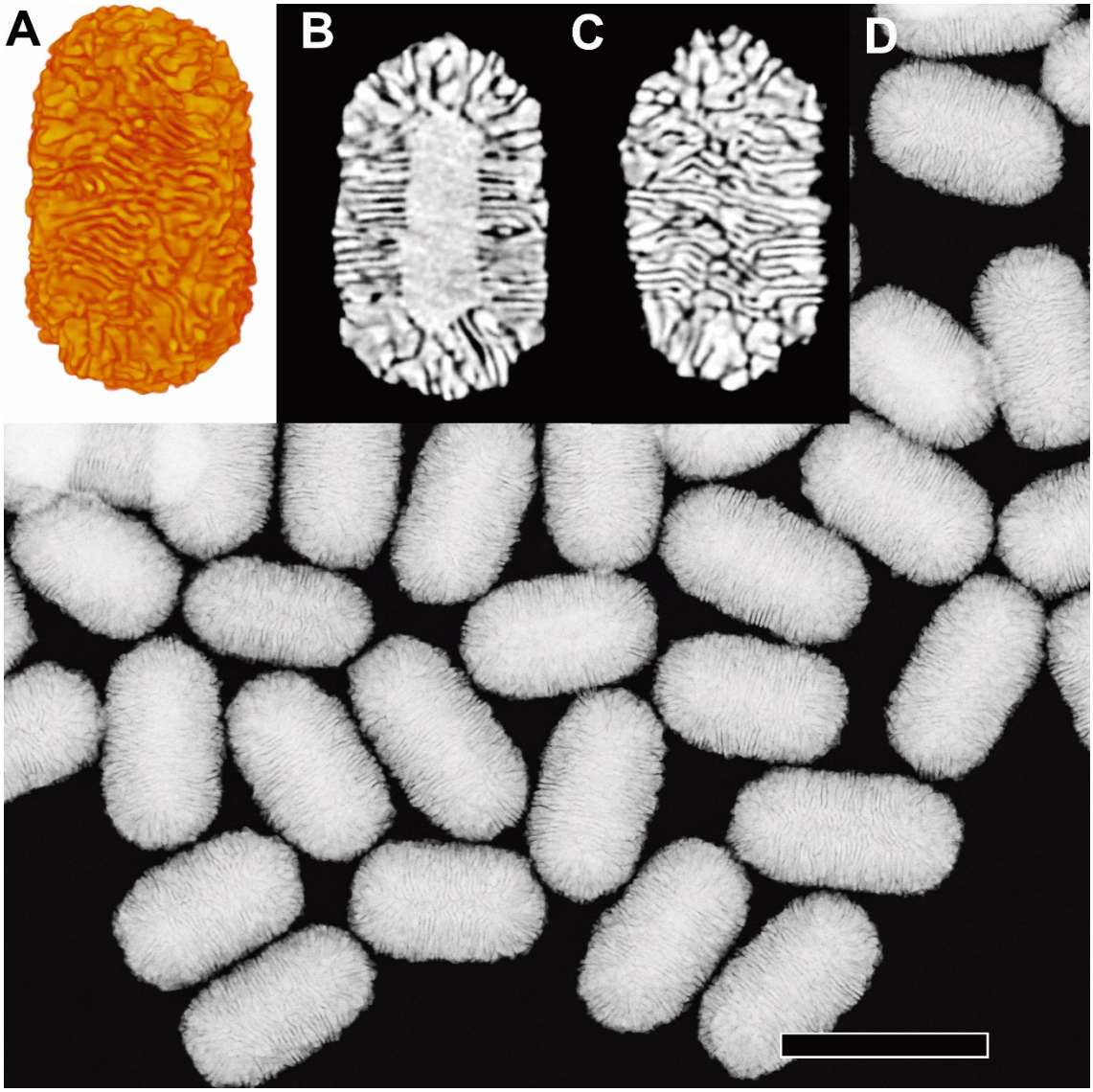

Fig. S9

HAADF-STEM and electron tomography reconstruction of chiral gold nanorods (210 nm long; 112 nm wide) synthesized in (*S*)-BINAMINE/CTAC. The 3D visualization of the electron tomography reconstruction (A) and orthoslices through the 3D reconstruction (B,C) enable investigation of their surface and the 3D morphology. Scale bar in D: 200 nm.

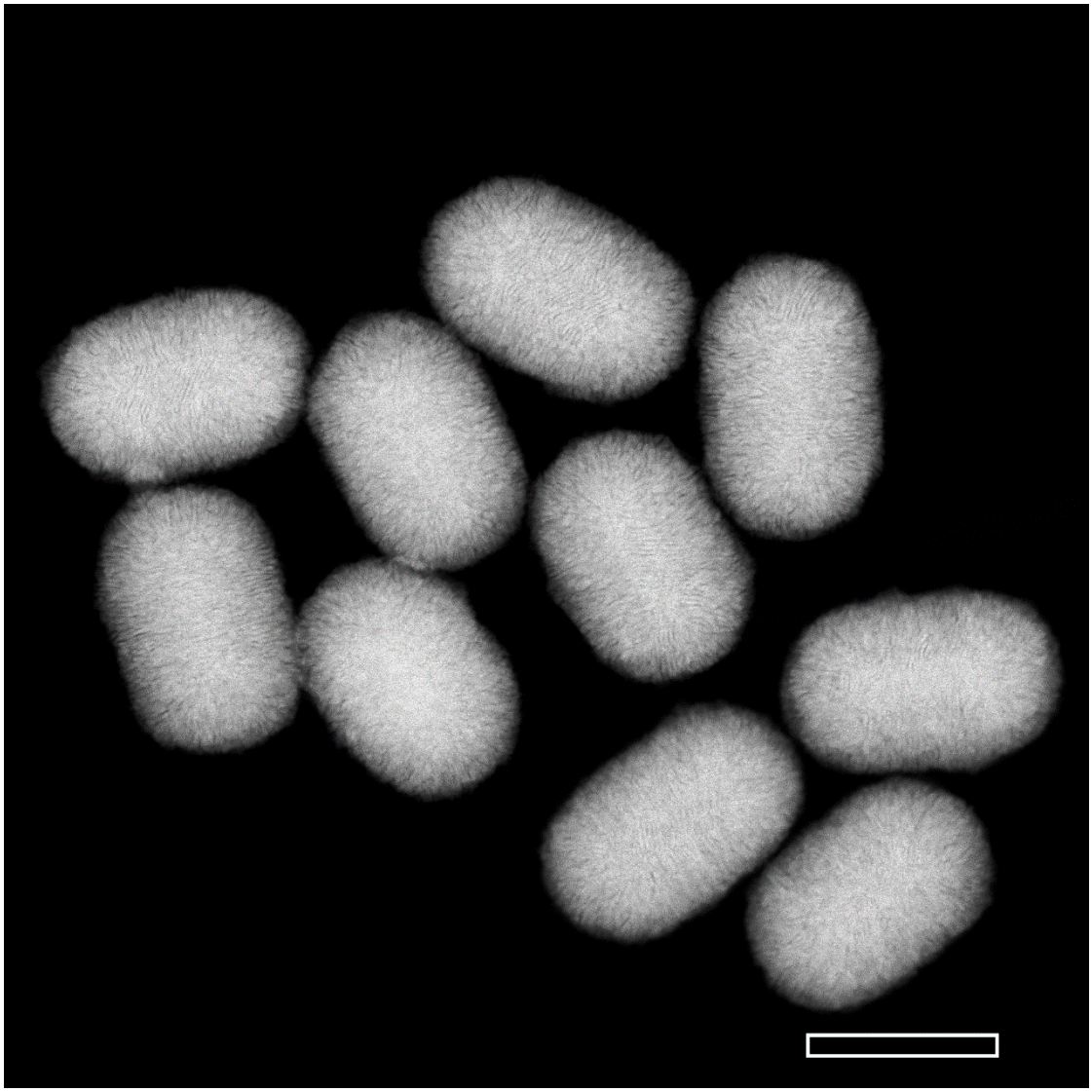

Fig. S10
HAADF-STEM image of chiral gold nanorods (270 nm long; 175 nm wide) synthesized in (*R*)-BINAMINE/CTAC. Scale bar: 200 nm.

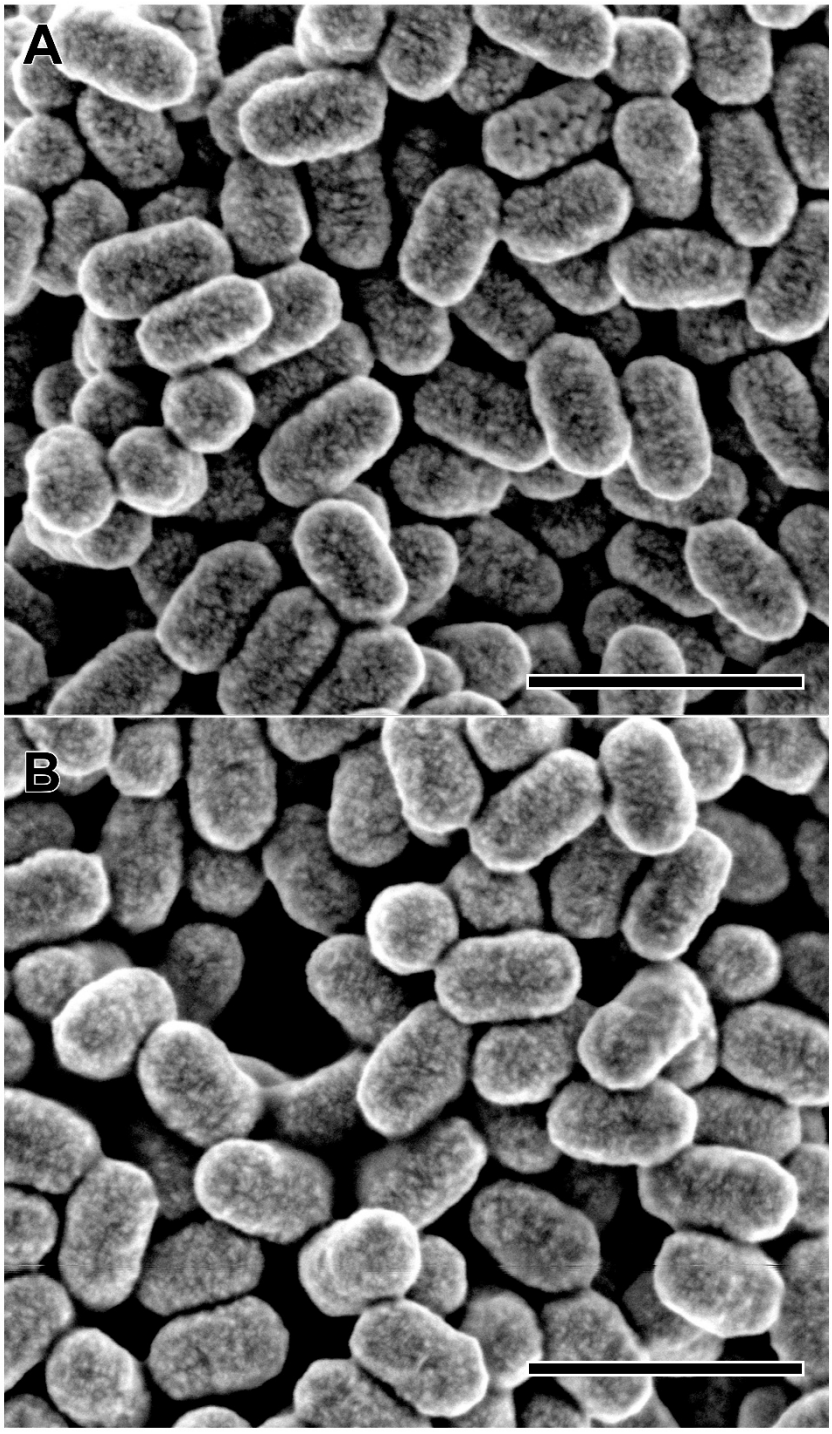

Fig. S11

SEM characterization of chiral gold nanorods (210 nm long; 112 nm wide) synthesized in (*R*) and (*S*)-BINAMINE/CTAC (A,B)**.** Scale bars: 400 nm.

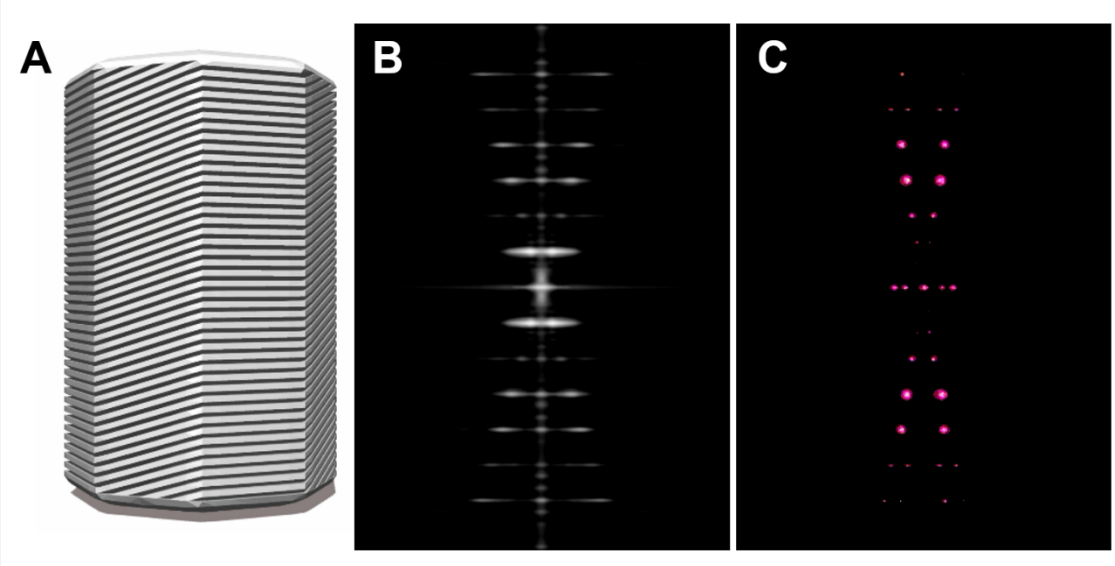

Fig. S12

Analysis of the Fourier transform of an idealized helical morphology. The original model is presented in (A), and the corresponding 3D FFT in (B). After segmenting the main diffraction spots, an X-shape can be clearly seen (C). These results are also presented in Movies S31-S35.

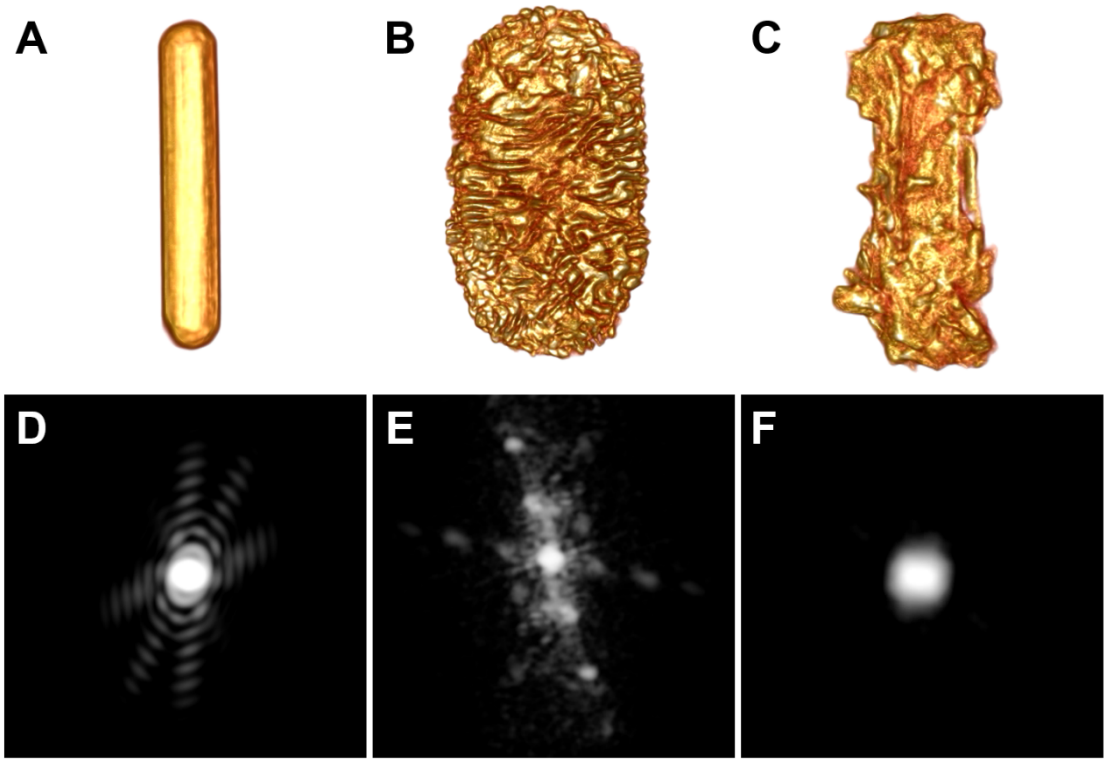

Fig. S13

Comparison between the Fourier transforms for experimental systems with a different degree of helicity. 3D reconstructions of a smooth gold nanorod (A), a chiral gold nanorod grown in (R)-BINAMINE/surfactant mixture (B), and a chiral gold nanorod prepared in (R)-BINOL/CTAC (C). The corresponding 3D FFT patters are provided in (D), (E) and (F), respectively. Please note that in (D) all diffraction spots in a single plane (see Movie S38), corresponding to the periodicity of the surface, whereas (E, see also Movie S10) shows a close resemblance with the 3D FFT in Fig. S12B. In the 3D FFT in (F, see also Movie S41), no clear diffraction spots can be observed, due to a lack of periodicity and chiral features.

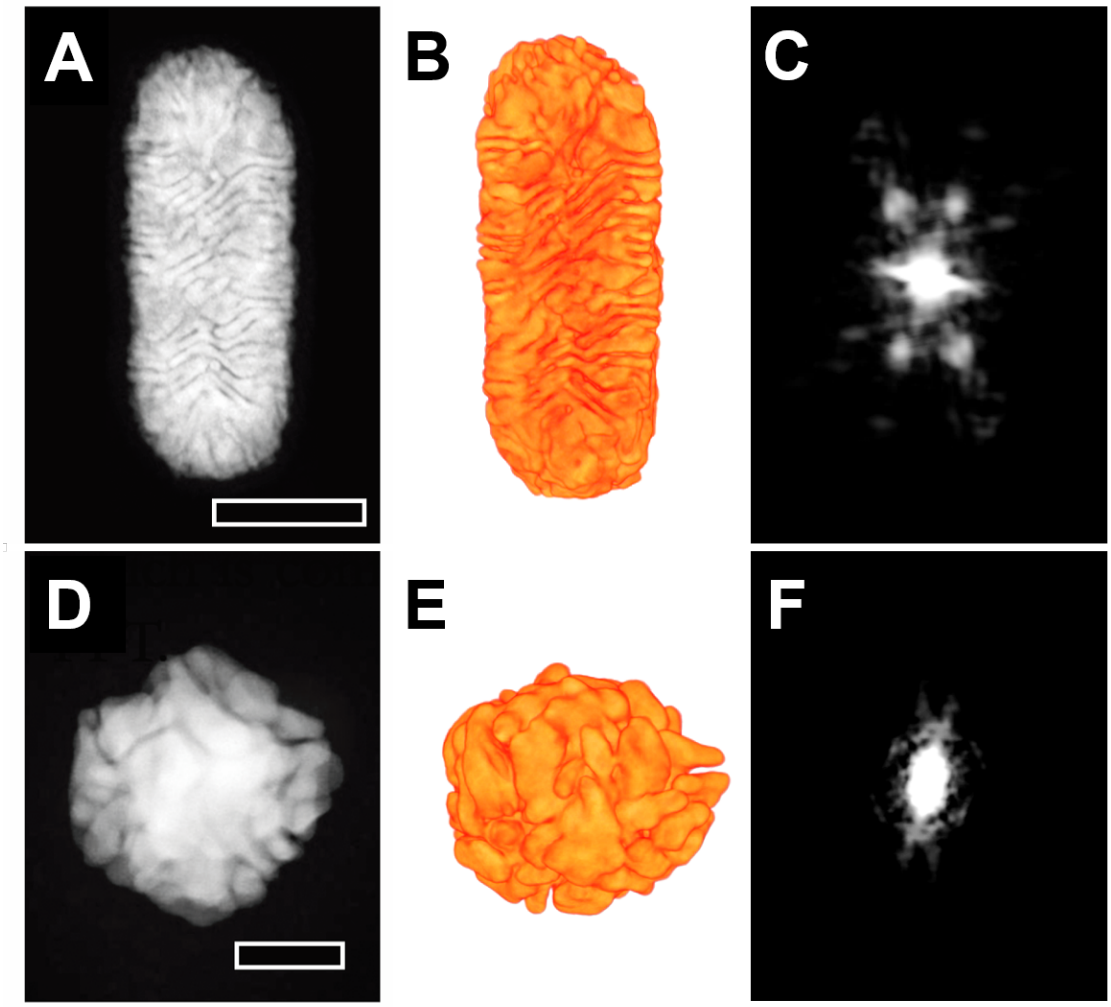

Fig. S14

Chiral morphology of gold nanorods and nanospheres. HAADF-STEM characterization of the chiral morphology of gold nanorods (A-C) and gold nanospheres (D-F). Acquisition of HAADF-STEM images series at different tilt angles enables obtaining the three-dimensional morphology of the nanoparticles (B,E). The Fourier transform of the 3D reconstructions of the gold nanorods (C) indicates an X-shaped pattern which is less obvious in the case of the spheres (F). Scale bar: 100 nm (A), 20 nm (D). Animated movies for the sphere are provided in Movies S43-S48.

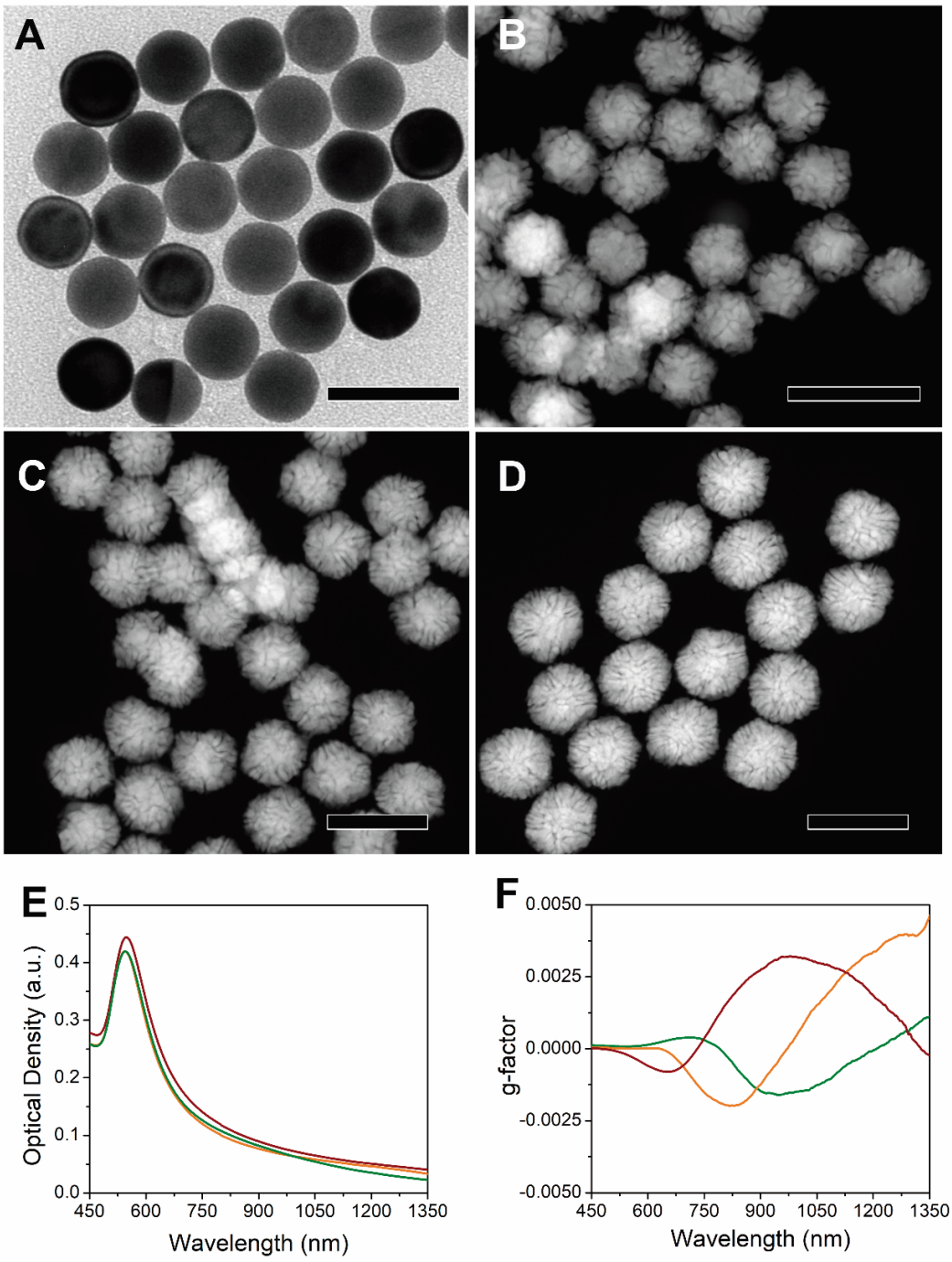

Fig. S15

Growth of chiral gold nanospheres by seeded growth on 30 nm spheres in (*R*)-BINAMINE/CTAC. TEM (A) and HAADF-STEM (B–D) images of 30 nm spheres (A), used to seed the growth of chiral gold nanospheres of 50 nm (B), 60 nm (C) and 70 nm (D) total diameter. UV-Vis-NIR (E) and dissymmetry (F) spectral evolution due to the increase of the chiral nanosphere size from 50 nm (brown), to 60 nm (orange) and 70 nm (olive). Scale bars: 50 nm (A), 100 nm (B–D).

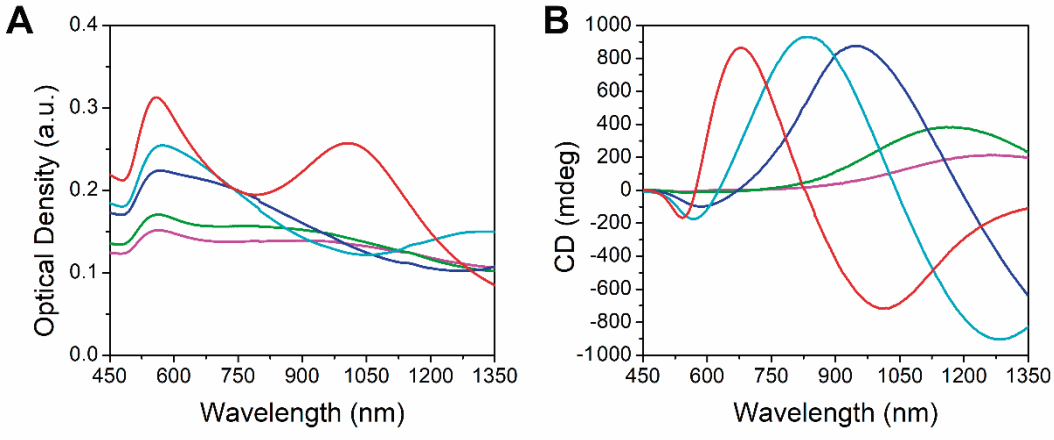

Fig. S16

Seeded growth on gold nanorods (130 nm long; 29 nm wide), in (*R*)-BINAMINE/CTAC. UV-Vis-NIR (A) and CD (B) spectra of the chiral nanorods with increasing dimensions: 165 × 73 nm (red), 200 × 92 nm (cyan), 210 × 112 nm (blue), 250 × 145 (green), 270 × 175 nm (magenta).

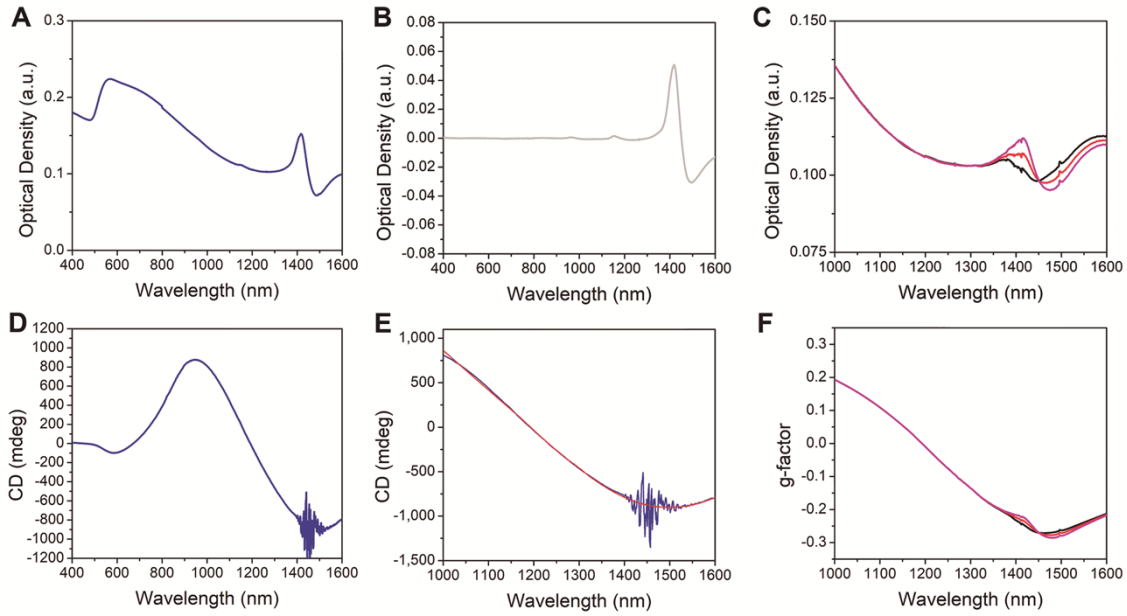

Fig. S17

Determination of anisotropy factor in the 1400-1500 nm wavelength range. (A, B) UV-Vis-NIR spectra of 210 × 112 nm chiral gold nanorods (A) and a CTAC solution (B), recorded up to 1600 nm. The shape of the noise around 1400 to 1500 nm is similar for both spectra. (C) As a result, it is possible to subtract the noise from spectra of chiral nanorods, using a factor to control the subtraction magnitude: 0.9 (black), 0.8 (red), 0.7 (magenta); i.e., we observe variations of instrumental noise intensity in different measurements. In the case of spectrum (D), a noise reduction can be made (E) by applying a Saviztky-Golay method (red). Thereby, approximate values of the anisotropy factor can be obtained (F), with only small observable changes, as a function of the noise subtraction factor (black: 0.9, red:0.8 and magenta: 0.7).

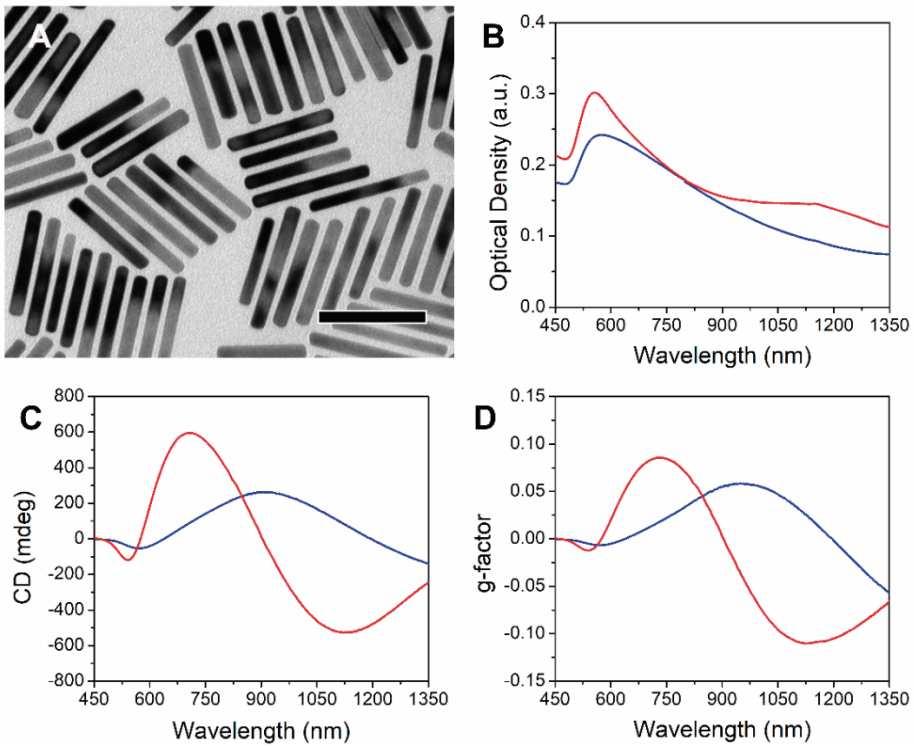

Fig. S18

Seeded growth on gold nanorods (100 nm long; 12 nm wide), in (*R*)-BINAMINE/CTAC. (A) TEM images of gold nanorods used as seeds. (B-D) UV-Vis-NIR (B), CD (C) and anisotropy factor (D) spectra for chiral nanorods obtained at two different seed concentrations: $3.1 \cdot 10^{-11}$ M (red) and $7.45 \cdot 10^{-12}$ M (blue).

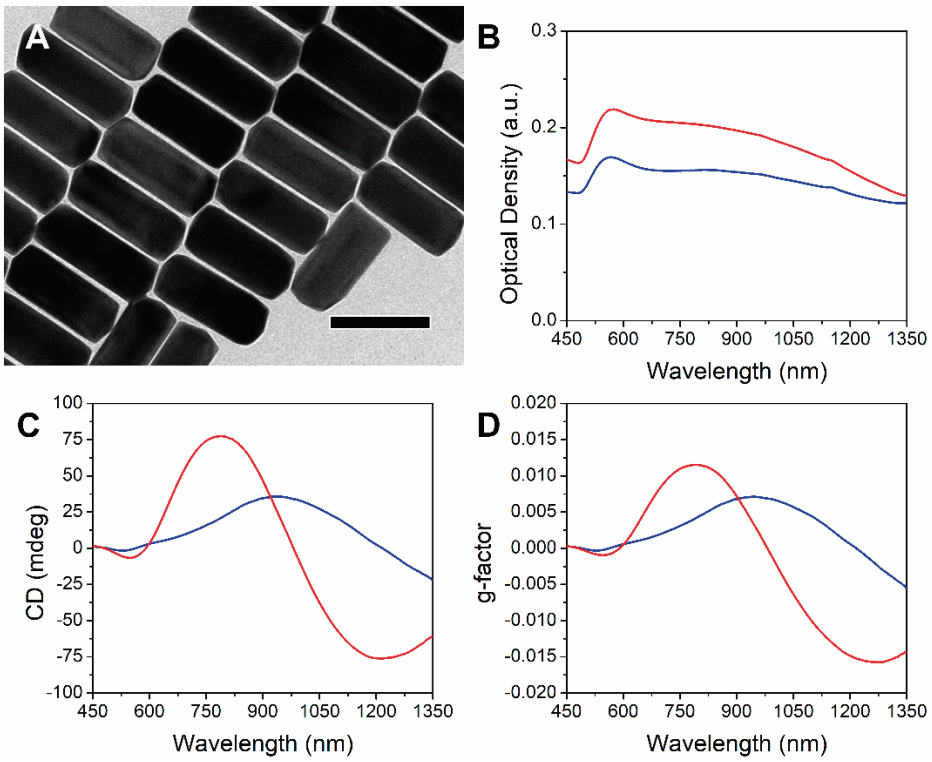

Fig. S19

Seeded growth on gold nanorods (135 nm long; 52 nm wide), in (*R*)-BINAMINE/CTAC. (A) TEM images of gold nanorods used as seeds. (B-D) UV-Vis-NIR (B), CD (C) and anisotropy factor (D) spectra for chiral nanorods obtained at two different seed concentrations: $1.2 \cdot 10^{-12}$ M (red) and $2.45 \cdot 10^{-12}$ M (blue).

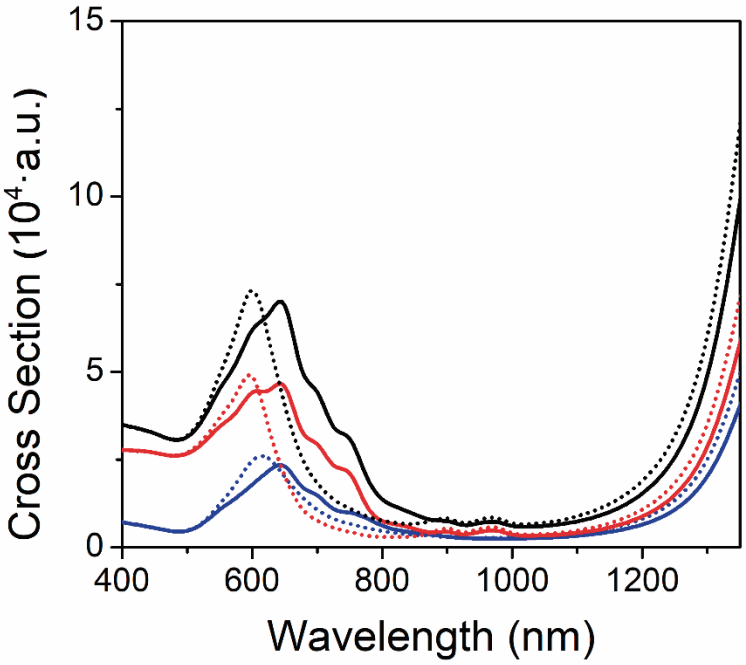

Fig. S20

Calculated LSPR bands for chiral gold nanorods: 175 long, 73 nm wide.
(A) Scattering (red), absorption (blue), and extinction (black) cross sections calculated for irradiation with left (solid) and right (dotted) circularly polarized light.

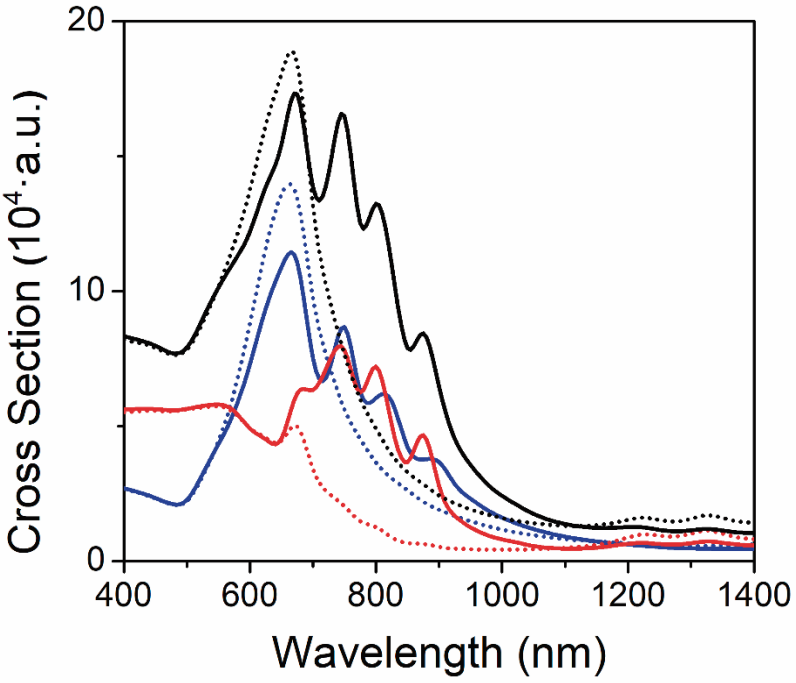

Fig. S21

Calculated LSPR bands for chiral gold nanorods: 210 nm long, 112 nm wide.
(A) Scattering (red), absorption (blue), and extinction (black) cross sections calculated for irradiation with left (solid) and right (dotted) circularly polarized light.

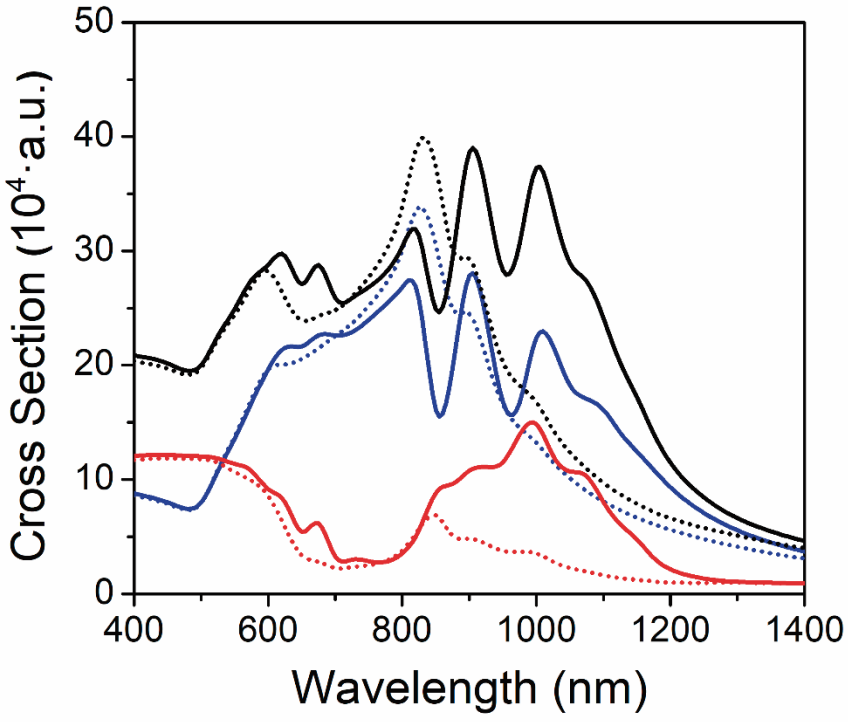

Fig. S22

Calculated LSPR bands for chiral gold nanorods: 270 long, 175 nm wide.
(A) Scattering (red), absorption (blue), and extinction (black) cross sections calculated for irradiation with left (solid) and right (dotted) circularly polarized light.

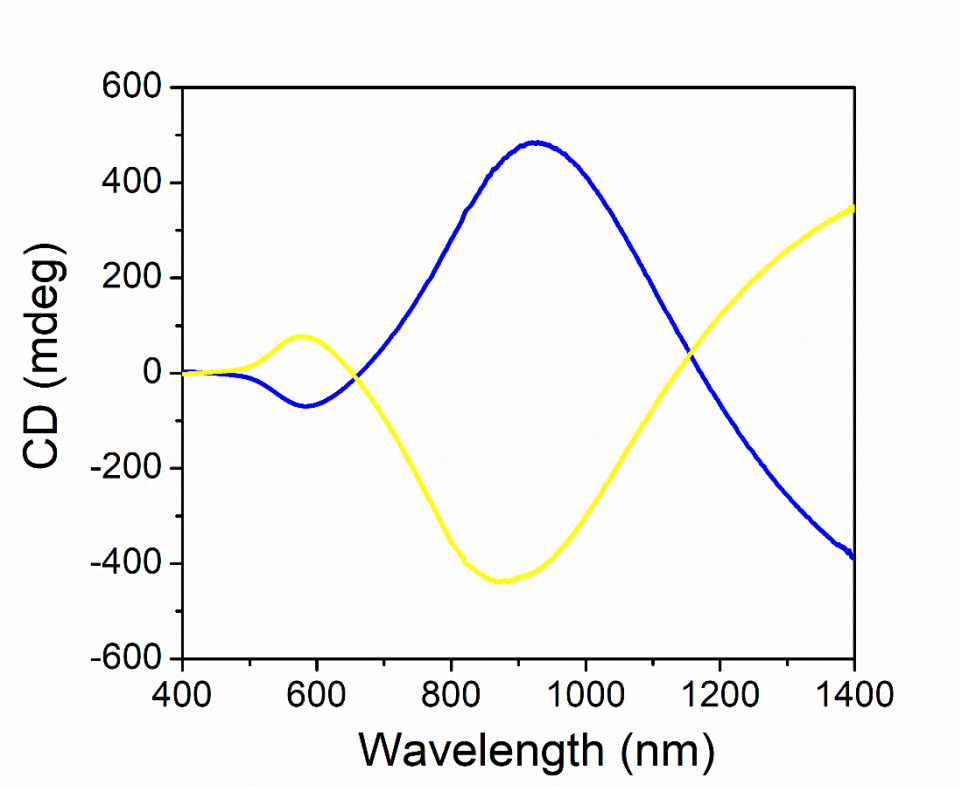

Fig. S23

Replacement of BINAMINE. Functionalization of the chiral nanorods with L-cysteine (i.e., a chiral molecule that replaces BINAMINE) once the growth reaction is completed did not modify the CD signal obtained for chiral gold nanorods synthesized with either (*R*)-BINAMINE (blue) or (*S*)-BINAMINE (yellow), as it would be expected if the chiroptical properties would arise from the coupling of the BINAMINE with the nanoparticle plasmon.

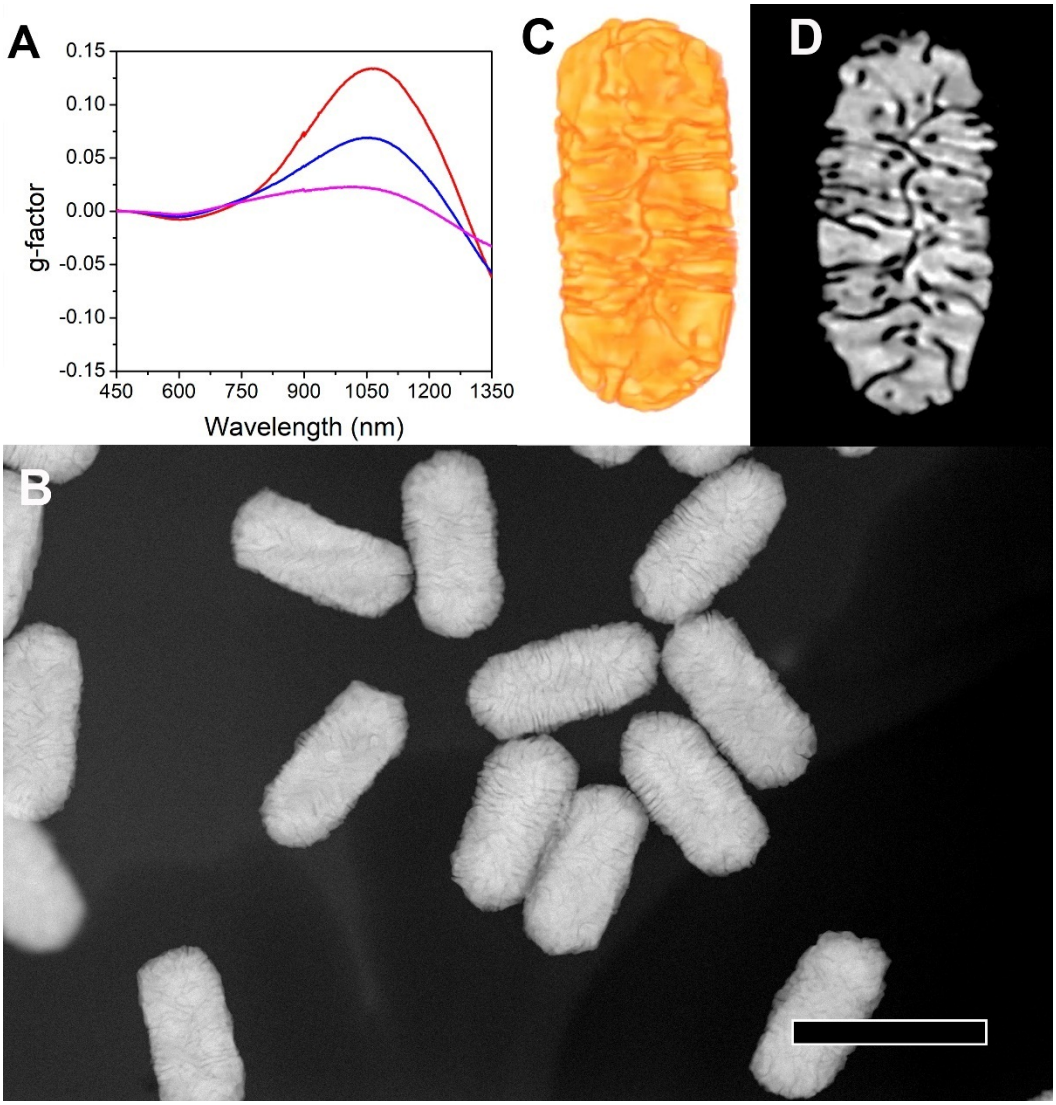

Fig. S24

Effect of ascorbic acid concentration on the growth of chiral gold nanorods in (*R*)-BINAMINE/CTAC, using 130 x 29 nm gold nanorod seeds. (A) Dissymmetry factor spectra of chiral gold nanorods obtained at different concentrations of ascorbic acid: 160 mM (red), 16 mM (blue) and 1.6 mM (magenta). (B) Low magnification HAADF-STEM image, and (C,D) electron tomography reconstruction of the chiral gold nanorods prepared at 1.6 mM of ascorbic acid: the 3D visualization of the electron tomography reconstruction (C) and orthoslices through the 3D reconstruction (D) enable investigation of the surface and 3D morphology. Scale bar in C: 200 nm.

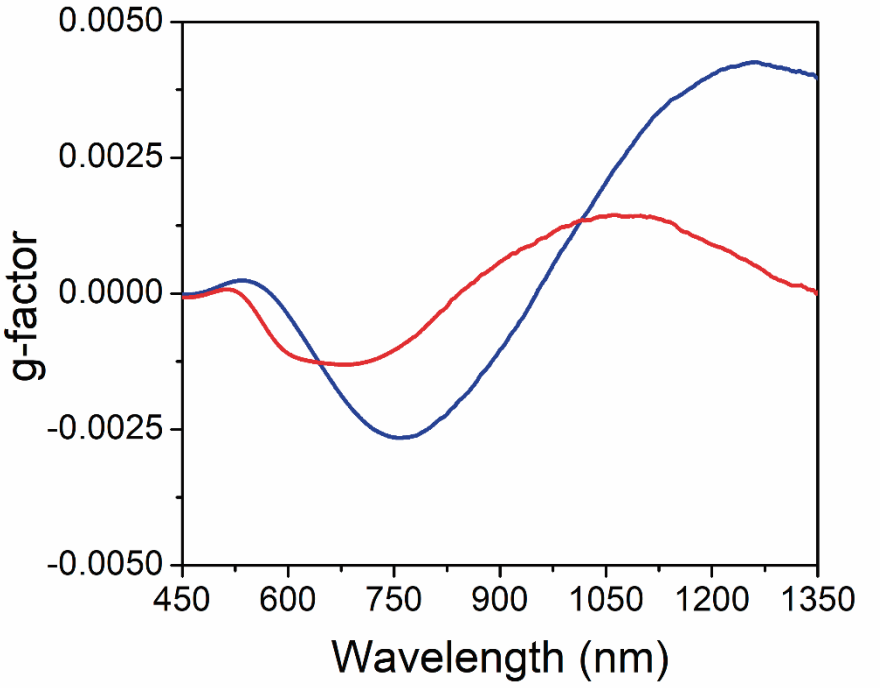

Fig. S25

Effect of replacing one amine with a hydroxyl group in BINAMINE, on the growth of chiral gold nanorods. Dissymmetry factor spectra of chiral gold nanorods obtained using (*R*)-(+)-2′-Amino-1,1′-binaphthalen-2-ol, instead of (*R*)-BINAMINE as co-surfactant, at two different nanorod seed (130 × 29 nm) concentrations: $2.3 \cdot 10^{-12}$ M (blue) and $4.6 \cdot 10^{-12}$ M (red).

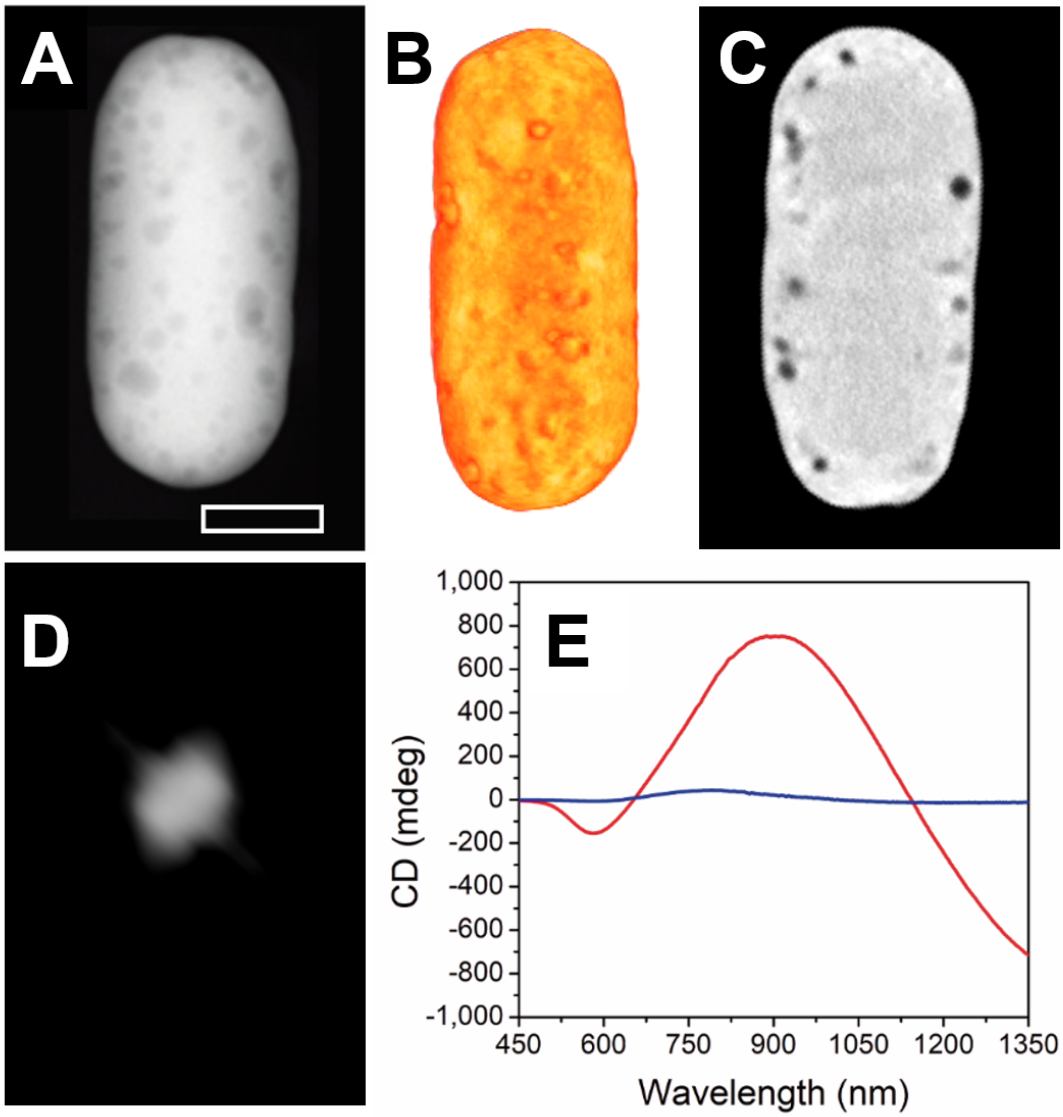

Fig. S26

Instability of chiral features. (A) HAADF-STEM image, (B) 3D visualization of the electron tomography reconstruction and (C) selected orthoslices through the 3D reconstruction of chiral gold nanorods, 2 weeks after synthesis, showing loss of chiral features when no cysteine is used to stabilize them. The Fourier transform of the reconstructed gold nanorods shows an achiral pattern. (E) Dissymmetry factor spectra of chiral gold nanorods obtained right after (red) and 11 days after synthesis (blue). Scale bar: 50 nm.

Table S1.
Growth conditions for gold nanorod synthesis with different dimensions.

LSPR	*AR*	*$AgNO_3$ (µL)*	*1M HCl (mL)*	*Seed (µL)*	*Length (nm)*	*Width (nm)*
762nm	2.5	1500	3	15	135 ± 12	52 ± 4
930nm	5.0	1500	12	45	130 ± 10	29 ± 3
1220nm	8.5	1500	10	500	100 ± 7	12 ± 1

Table S2.
Co-surfactant mass weighed for the preparation of 2.5 mM solution.

Co-surfactant	***Mass(mg)***
BINOL	35.79
BINAMINE	35.55
***(R)*-(+)-2′-Amino-1,1′-binaphthalen-2-ol**	35.66

Table S3.
Co-surfactants and nanoparticles size, shape and concentration used for the growth of chiral gold nanoparticles.

Figure	*NPs*	*Co-surfactant*	*Size LxW (nm)*	*Volume (µL/mL growth solution)*	*[NP] M*
2B, S4, S5, S13C,F	Nanorods	(*R*)-BINOL	130 × 29	6.8	$1.4 \cdot 10^{-12}$
3E-H, S16				15	$3.2 \cdot 10^{-12}$
2C, 2F,G, 3A-D, 4A-blue, S8, S11A,S13B, S13E, S16-blue, S17, S23-blue, S24, S26		(*R*)-BINAMINE		13.5	$2.9 \cdot 10^{-12}$
S9, S11B, S23-yellow		(*S*)-BINAMINE			
2D,E, 4A-red, S7, S14A-C, S16-red		(*R*)-BINAMINE		38	$8.1 \cdot 10^{-12}$
S16-cyan				20.5	$4.4 \cdot 10^{-12}$
S16-green				6.8	$1.45 \cdot 10^{-12}$
2H,I, 4A-magenta, S10, S16-magenta				4.0	$8.5 \cdot 10^{-13}$
2J,K, S14D-F, S15B,E,F-brown	Nanospheres		30	29,6	$1.76 \cdot 10^{-10}$
S15C,E,F -orange				14,8	$8.8 \cdot 10^{-11}$
S15D,E,F -olive				7.4	$4.4 \cdot 10^{-11}$
S18-red	Nanorods		100 × 12	4.2	$3.1 \cdot 10^{-11}$
S18-blue				1.0	$7.45 \cdot 10^{-12}$
S19-red			135 × 52	21.7	$2.45 \cdot 10^{-12}$
S19-blue				10.8	$1.2 \cdot 10^{-12}$
S25-red		(*R*)-2′-Amino-1,1′-binaphthalen-2-ol	130 × 29	20.8	$4.6 \cdot 10^{-12}$
S25-blue				10.4	$2.3 \cdot 10^{-12}$

Table S4.
Forcefield employed in MD simulations for Coulomb and van der Waals interactions. C6 and C12 are Lennard-Jones coefficients for united-atom interactions as input in Gromacs. The charges, q, are given in electronic unit charges.

Molecule or Atom	*Group*	C_6 / kJ mol^{-1} nm^6	C_{12} / kJ mol^{-1} nm^{12}	*q / e*
CTA^+	CH_2	0.0074684164	$3.3965584\ 10^{-5}$	0.303
	N	0.0024364096	$2.319529\ 10^{-6}$	-0.359
	CH_3	0.0096138025	$2.6646244\ 10^{-5}$	0.352
BINOL	O	0.0022619536	$1.505529\ 10^{-6}$	$-0.249^{(5)}$
	H	0.0	0.0	$0.249^{(5)}$
BINAMINE	N	0.0024364096	$2.319529\ 10^{-6}$	$-0.414^{(5)}$
	H	0.0	0.0	$0.207^{(5)}$
Au		0.029227046	$0.9650000\ 10^{-5}$	0
Cl^-		0.01380625	0.0001069156	-1
Na^+		$7.2063121\ 10^{-5}$	$2.1025\ 10^{-8}$	+1

Table S5.
Detailed information on system size and number of molecules for micelles simulated in solution.

System	*N CTAC*	*N BINOL*	*N WATER*	*N NaCl*	*Box dimensions / nm*
(*S*)-10 nm	200	20	25480	2000	9.9783 ´ 9.9783 ´ 9.9783
(R)-10 nm	200	20	25480	2000	9.9784 ´ 9.9784 ´ 9.9784
(*S*)-30 nm	600	60	76440	6000	9.9787 ´ 9.9787 ´ 29.9362
(R)-30 nm	600	60	76440	6000	9.9784 ´ 9.9784 ´ 29.9354
(*S*)-60 nm	1200	120	152880	12000	9.9788 ´ 9.9788 ´ 59.8731
(R)-60 nm	1200	120	152880	12000	9.9788 ´ 9.9788 ´ 59.8731
		N BINAMINE			
(*S*)-60 nm	1200	120	152880	12000	9.9805 ´ 9.9805 ´ 59.8829
(R)-60 nm	1200	120	152880	12000	9.9799 ´ 9.9799 ´ 59.8796
CTAC	200		25480	2000	9.9547 ´ 9.9547 ´ 9.9547

Table S6.
Systems details for MD simulations with gold nanorod.

System	*N CTAC*	*N BINOL*	*N WATER*	*N Au*	*Box dimensions / nm*
(*S*)-BINOL/CTAC	15000	1500	2034235	350000	41.8637 × 41.8637 × 52.1668
(R)-BINOL/CTAC	15000	1500	2035862	350000	41.8793 × 41.8793 × 52.1668
CTAC	15000	0	2054518	350000	41.8690 × 41.8690 × 52.1668

Movie S1

Colored visualization of a 3D reconstruction of a chiral gold nanorod grown using a (*R*)-BINAMINE/surfactant mixture (165 nm long, 73 nm wide). The reconstruction was obtained by HAADF-STEM tomography and shows a complex surface containing sharp wrinkles.

Movie S2

Greyscale visualization of a 3D reconstruction of a chiral gold nanorod grown using a (*R*)-BINAMINE/surfactant mixture (165 nm long, 73 nm wide). The reconstruction was obtained by HAADF-STEM tomography and shows a complex surface containing sharp wrinkles around the central gold nanorod.

Movie S3

Slices through the 3D reconstruction of a chiral gold nanorod grown using a (*R*)-BINAMINE/surfactant mixture (165 nm long, 73 nm wide). The reconstruction was obtained by HAADF-STEM tomography. In the slices, the central old nanorod can be clearly distinguished from the shell of wrinkles.

Movie S4

Visualization of a Fast Fourier Transformation of a 3D reconstruction of a chiral gold nanorod grown using (*R*)-BINAMINE/surfactant mixture (165 nm long, 73 nm wide).

Movie S5

Visualization of a Fast Fourier Transformation of a 3D reconstruction of a chiral gold nanorod grown using a (*R*)-BINAMINE/surfactant mixture (165 nm long, 73 nm wide), in which the diffraction spots are segmented.

Movie S6

Visualization of the result of applying an inverse FFT on the segmented 3D FFT shown in Movie S5. The inverse FFT is superimposed with the original 3D reconstruction. These results are obtained for a chiral gold nanorod grown using a (*R*)-BINAMINE/surfactant mixture.

Movie S7

Colored visualization of a 3D reconstruction of a chiral gold nanorod grown using a (*R*)-BINAMINE/surfactant mixture (210 nm long, 112 nm wide). The reconstruction was obtained by HAADF-STEM tomography and shows a complex surface containing sharp wrinkles.

Movie S8

Greyscale visualization of a 3D reconstruction of a chiral gold nanorod grown using a (*R*)-BINAMINE/surfactant mixture (210 nm long, 112 nm wide). The reconstruction was obtained by HAADF-STEM tomography and shows a complex surface containing sharp wrinkles around the central Au nanorod.

Movie S9

Slices through the 3D reconstruction of a chiral gold nanorod grown using a (*R*)-BINAMINE/surfactant mixture (210 nm long, 112 nm wide). The reconstruction was obtained by HAADF-STEM tomography. In the slices, the central old nanorod can be clearly distinguished from the shell of wrinkles.

Movie S10

Visualization of a Fast Fourier Transformation of a 3D reconstruction of a chiral gold nanorod grown using (*R*)-BINAMINE/surfactant mixture (210 nm long, 112 nm wide).

Movie S11

Visualization of a Fast Fourier Transformation of a 3D reconstruction of a chiral gold nanorod grown using a (*R*)-BINAMINE/surfactant mixture (210 nm long, 112 nm wide), in which the diffraction spots are segmented.

Movie S12

Visualization of the result of applying an inverse FFT on the segmented 3D FFT shown in Movie S11. The inverse FFT is superimposed with the original 3D reconstruction. These results are obtained for a chiral gold nanorod grown using a (*R*)-BINAMINE/surfactant mixture.

Movie S13

Greyscale visualization of a 3D reconstruction of a chiral gold nanorod grown using a (*S*)-BINAMINE/surfactant mixture (210 nm long, 112 nm wide). The reconstruction was obtained by HAADF-STEM tomography and shows a complex surface containing sharp wrinkles around the central gold nanorod.

Movie S14

Slices through the 3D reconstruction of a chiral gold nanorod grown using a (*S*)-BINAMINE/surfactant mixture (210 nm long, 112 nm wide). The reconstruction was obtained by HAADF-STEM tomography. In the slices, the central old nanorod can be clearly distinguished from the shell of wrinkles.

Movie S15

Visualization of a Fast Fourier Transformation of a 3D reconstruction of a chiral gold nanorod grown using (*S*)-BINAMINE/surfactant mixture (210 nm long, 112 nm wide).

Movie S16

Visualization of a Fast Fourier Transformation of a 3D reconstruction of a chiral gold nanorod grown using a (*S*)-BINAMINE/surfactant mixture (210 nm long, 112 nm wide), in which the diffraction spots are segmented.

Movie S17

Visualization of the result of applying an inverse FFT on the segmented 3D FFT shown in Movie S16. The inverse FFT is superimposed with the original 3D reconstruction. These results are obtained for a chiral gold nanorod grown using a (*S*)-BINAMINE/surfactant mixture.

Movie S18

Colored visualization of a 3D reconstruction of a chiral gold nanorod grown using a (*R*)-BINAMINE/surfactant mixture (270 nm long, 175 nm wide). The reconstruction was obtained by HAADF-STEM tomography and shows a complex surface containing sharp wrinkles.

Movie S19

Greyscale visualization of a 3D reconstruction of a chiral gold nanorod grown using a (*R*)-BINAMINE/surfactant mixture (270 nm long, 175 nm wide). The reconstruction was obtained by HAADF-STEM tomography and shows a complex surface containing sharp wrinkles around the central Au nanorod.

Movie S20

Slices through the 3D reconstruction of a chiral gold nanorod grown using a (*R*)-BINAMINE/surfactant mixture (270 nm long, 175 nm wide). The reconstruction was obtained by HAADF-STEM tomography. In the slices, the central gold nanorod can be clearly distinguished from the shell of wrinkles.

Movie S21

Visualization of a Fast Fourier Transformation of a 3D reconstruction of a chiral gold nanorod grown using (*R*)-BINAMINE/surfactant mixture (270 nm long, 175 nm wide).

Movie S22

Visualization of a Fast Fourier Transformation of a 3D reconstruction of a chiral gold nanorod grown using a (*R*)-BINAMINE/surfactant mixture (270 nm long, 175 nm wide), in which the diffraction spots are segmented.

Movie S23

Visualization of the result of applying an inverse FFT on the segmented 3D FFT shown in Movie S22. The inverse FFT is superimposed with the original 3D reconstruction. These results are obtained for a chiral gold nanorod grown using a (*R*)-BINAMINE/surfactant mixture.

Movie S24

Colored visualization of the 3D reconstruction of a gold nanorod on which a chiral platinum shell was grown using (*R*)-BINOL/surfactant mixture. The reconstruction was obtained by HAADF-STEM tomography. Due to the similar Z number between platinum and gold, there is no contrast between both elements.

Movie S25

Visualization of the 3D elemental mapping of a gold nanorod on which a chiral platinum shell was grown using (*R*)-BINOL/surfactant mixture. The reconstruction was obtained by EDX tomography, so that platinum (in blue) and gold (in yellow) can be readily distinguished.

Movie S26

Greyscale visualization of the 3D reconstruction of a gold nanorod on which a chiral platinum shell was grown using (*R*)-BINOL/surfactant mixture. The reconstruction was obtained by HAADF-STEM tomography. Due to the similar Z number between platinum and gold, there is no contrast between both elements.

Movie S27

Slices through the 3D reconstruction of an Au nanorod on which a chiral platinum shell was grown using (*R*)-BINOL/surfactant mixture, obtained by HAADF-STEM tomography. The central gold rod and the platinum shell can be distinguished based on a difference in morphology.

Movie S28

Visualization of a Fast Fourier Transformation of a 3D reconstruction of a gold nanorod on which a chiral platinum shell was grown using (*R*)-BINOL/surfactant mixture. The spots in the Fourier space indicate periodicity at the surface of the nanorod.

Movie S29

Visualization of a Fast Fourier Transformation of a 3D reconstruction of a gold nanorod on which a chiral platinum shell was grown using (*R*)-BINOL/surfactant mixture. The diffraction spots were segmented. Due to the small distance between the spots, some features are merged in big spots, which contain the desired frequencies.

Movie S30

Visualization of the result when applying an inverse Fast Fourier Transformation on the segmented version of the 3D FFT as shown in movie S29. The inverse Fast Fourier Transformation is superimposed with the original 3D reconstruction.

Movie S31

3D visualization of the ideal helical model in fig. S12A.

Movie S32

Slices through the ideal helical model in fig. S12A.

Movie S33

Visualization of a Fast Fourier Transformation of the ideal helical model (fig. S12A). This corresponds to an animated version of fig. S12B.

Movie S34

Visualization of a Fast Fourier Transformation of the ideal helical model (fig. S12A). The diffraction spots were segmented. This corresponds to an animated version of the superposition of figs. S12, B and C.

Movie S35

Colored 3D visualization of the ideal helical model in fig. S12A.

Movie S36

3D visualization of the gold nanorod in fig. S13A.

Movie S37

Slices through the gold nanorod in fig. S13A.

Movie S38

Visualization of a Fast Fourier Transformation of the gold nanorod in Fig. S13A. It can be seen that all spots are in one plane. This corresponds to an animated version of fig. S13D.

Movie S39

Greyscale 3D visualization of a gold nanorod prepared in (*R*)-BINOL/CTAC (fig. S13C).

Movie S40

Slices through a gold nanorod prepared in (*R*)-BINOL/CTAC (fig. S13C).

Movie S41

Visualization of a Fast Fourier Transformation of a gold nanorod prepared in (*R*)-BINOL/CTAC. No spots other than the central spot are observed. This corresponds to an animated version of fig. S13F.

Movie S42

Visualization of the result of applying an inverse Fast Fourier Transformation on the segmented version of the 3D FFT. The inverse Fast Fourier Transformation is superimposed with the original 3D reconstruction. Only the global morphology of the nanorod is visible.

Movie S43

Colored 3D visualization of the gold nanosphere in fig. S14D. This corresponds to an animated version of fig. S14E.

Movie S44

Greyscale 3D visualization of the gold nanosphere in fig. S14D.

Movie S45

Slices through the gold nanosphere in fig. S14D.

Movie S46

Visualization of a Fast Fourier Transformation of the gold nanosphere in fig. S14D. This corresponds to an animated version of fig. S14F.

Movie S47

Visualization of a Fast Fourier Transformation of the gold nanosphere in fig. S14D. The diffraction spots were segmented.

Movie S48

Visualization of the result of applying an inverse Fast Fourier Transformation on the segmented version of the 3D FFT, as shown in movies S46 and S47. The inverse Fast Fourier Transformation is superimposed with the original 3D reconstruction. Although some chiral features can be observed, the spheres yield a more random wrinkle organization.